Fuel 253 (2019) 1114–1129

Contents lists available at ScienceDirect

Fuel

journal homepage: www.elsevier.com/locate/fuel

Full Length Article

Modelling and optimization of enhanced coalbed methane recovery using CO_2/N_2 mixtures

Chaojun Fan[a,b,c,*], Derek Elsworth[c], Sheng Li[a,*], Zhongwei Chen[c,d], Mingkun Luo[a,e], Yu Song[c], Haohao Zhang[a]

[a] College of Mining, Liaoning Technical University, Fuxin 123000, China
[b] State Key Laboratory Cultivation Base for Gas Geology and Gas Control, Henan Polytechnic University, Jiaozuo 454003, China
[c] Energy and Mineral Engineering, G3 Center and EMS Energy Institute, Pennsylvania State University, University Park, PA, USA
[d] School of Mechanical and Mining Engineering, The University of Queensland, St Lucia, QLD 4072, Australia
[e] Center of Technology, Shanxi Lu'an Mining (Group) Limited Liability Company, Changzhi 046299, China

ARTICLE INFO

Keywords:
Enhanced CBM recovery
Injection of gas mixture
Thermo-hydro-mechanical coupling model (THM)
Mass and heat transfer
Variable-composition
CO_2 sequestration

ABSTRACT

Injection of gas mixtures (CO_2, N_2) into coal seams is an efficient method to both reduce CO_2 emissions and increase the recovery of coalbed methane. This process involves a series of complex interactions between ternary gases (CH_4, CO_2, and N_2) co-adsorption on coals, mass transport of two-phase flow, together with heat transfer and coal deformation. We develop an improved thermo-hydro-mechanical (THM) model coupling these responses for gas mixture enhanced CBM recovery (GM-ECBM). The model is first validated, and then applied to simulate and explore the evolution of key parameters during GM-ECBM recovery. Schedules of constant- and variable-composition injection are optimized to maximize CH_4 recovery and CO_2 sequestration. Result shows that the injected gas mixture displaces CH_4 through competitive sorption and accelerates the transport of CH_4 within the coal seam. The consistency between the modelling and field results verifies the feasibility and fidelity of the THM model for effective simulation key processes in GM-ECBM. Permeability evolution is strongly influenced by the combined effects of CH_4 desorption induced matrix shrinkage, CO_2/N_2 adsorption induced matrix swelling, thermal strains, and compaction induced by changes in effective stress. During ECBM, reservoir permeability first increases due to pressure depletion and CH_4 desorption, then dramatically decreases due to matrix swelling activated by the arrival of the CO_2/N_2 mixture. CH_4 pressure decreases rapidly at early time due to displacement by the injected gas mixture, and then deceases slowly in the later stage. The sweep of N_2 accelerates CH_4 desorption and subsequent transport, and hence promotes a decrease in reservoir temperatures distant from the injection well even prior to the arrival of CO_2. CH_4 production rate during GM-ECBM exhibits a decline-increase-decline trend and usually has an elevated but delayed CH_4 production peak compared to primary recovery. A higher CO_2 Langmuir strain constant reduces the critical CO_2 composition in the injected mixture when reaching the threshold of well shut down. An improved balance between early threshold (N_2) and large matrix swelling (CO_2) can be achieved by injection beginning with low CO_2 composition and following with a sequential increase of CO_2 composition. In studied cases, the gas recovery ratio of the optimal variable-composition case reaches 68.4% compared to of 59.4% pure CO_2 and 64.2% of optimal constant-composition cases, indicating a higher efficiency of variable-composition injection.

1. Introduction

Coalbed methane (CBM) recovered from unconventional reservoirs is an important source of energy that accounts for approximately 6–9% of the current natural gas production [1–3]. CBM is also recovered to improve safety during coal mining and in particular to prevent gas explosions, coal and gas outbursts [4–6]. In both cases, CBM is recovered by boreholes to the surface [7]. However, the methane recovery rate driven by natural pressure depletion reduces rapidly due to the sharp decrease of reservoir pressure around the wellbore [3,8]. Co-injection of other gases into the coal seam is an efficient approach to increase CBM recovery through competitive adsorption and in maintaining reservoir pressure to prevent the closure of coal fractures [9,10]. Gases commonly used as injectants are nitrogen (N_2), carbon

* Corresponding authors at: College of Mining, Liaoning Technical University, Fuxin 123000, China. (S. Li)
E-mail addresses: chaojunfan@139.com (C. Fan), lisheng76@139.com (S. Li).

https://doi.org/10.1016/j.fuel.2019.04.158
Received 12 January 2019; Received in revised form 13 April 2019; Accepted 28 April 2019
0016-2361/

dioxide (CO_2), and binary mixtures of these gases (N_2/CO_2) [11–13].

As an effective technology for carbon utilization, enhanced coalbed methane (ECBM) with CO_2 injection has significant potential for the reduction of CO_2 emission [14–16]. The CH_4 recovery rate may be increased (~30%), as apparent in field, experiments and numerical simulations of CO_2 injection compared against natural depletion [17–19]. However, pure CO_2 injection may lead to dramatic drop of reservoir permeability due to the significant matrix swelling resulting from the greater adsorption affinity of CO_2 to coal, than N_2 and CH_4 [20–22]. This reduction in permeability (normally in the range of one to two orders of magnitude) will reduce the injectivity and productivity in wells [23,24]. Therefore, the injection of a binary gas mixture (N_2/CO_2) may be used to prevent permeability reduction by alleviating matrix swelling and to thereby increase the injection rate during CO_2-ECBM [25,26]. This has been proven effective in enhancing methane recovery in several field applications [11,27,28].

Gas-mixture enhanced coalbed methane recovery (GM-ECBM) involves interactions among the ternary gases (CH_4, CO_2, and N_2), co-adsorption, gas diffusion in the matrix, gas-water two-phase flow in fractures, heat transfer, and coal deformation [29–32]. These complex processes render field and laboratory tests essentially non-repeatable [33,34]. Numerical simulations may be applied to yield scientific insight into the processes controlling gas injection ECBM recovery [35–37]. The simulation of gas injection in coalbeds was first carried out to investigate overall performance during injection [38]. The feasibility of CO_2-ECBM recovery has been investigated by combining the essential features of infiltration and diffusion of binary gases (CO_2, CH_4), competitive sorption and deformation [39] and in examining the impacts of N_2 injection, [40] pre-drainage of formation water and non-isothermal adsorption for the evaluation of gas production [41–43]. In recent studies, these two factors were taken into consideration in simulations [44,45]. In general, these studies provide a useful theoretical foundation for gas injection enhanced CBM recovery, although some important factors are still overlooked, as shown in Table 1. Therefore, a fully coupled model for GM-ECBM has some utility in defining the full suite of interactions.

Due to the low sorption capacity and low dynamic viscosity of N_2, rapid and dramatic response of CH_4 production has been observed in N_2-ECBM pilots [47]. However, early N_2 breakthrough may also result, which may require early well shutdown due to contamination by N_2 of produced gas. This early N_2 breakthrough has been confirmed by several experiments, simulations and field tests [19,24,25,27]. Hence, the composition of the injected gas mixture (N_2, CO_2) has a significant impact on ultimate CH_4 recovery. An optimal composition for the N_2/CO_2 mixture injection may be found to balance early N_2 breakthrough and excessive matrix swelling induced by CO_2 adsorption, and prolong the process of economic CH_4 recovery together with CO_2 sequestration in coal.

The following describes an improved thermo-hydro-mechanical (THM) coupling model for simulating GM-ECBM recovery, including the interactions of ternary gases non-isothermal co-adsorption, mass transport by diffusion in matrix and two-phase flow in fractures, and thermal transfer, as well as the coupling of these fields with the evolution of porosity and permeability. This model is firstly validated by history matching *in situ* observation. Then, the evolutions of key parameters during GM-ECBM recovery are explored. Finally, the recovery schedules of constant- and variable-composition are optimized to determine the optimal composition for gas mixture injection.

2. Thermo-hydro-mechanical coupled model for GM-ECBM recovery

GM-ECBM involves injection of a ternary gas mixture (CH_4, CO_2, and N_2) that promotes co-adsorption on the coal matrix, and mass migration in the form of gas-water two-phase flow, heat transfer (thermal conduction and convection) driven by the injected gas mixture, together with coal deformation induced by the change in effective stress, gas sorption and reservoir temperature. The complex interactions among these processes are manifest in the response to thermo-hydro-mechanical (THM) coupling. Here, we establish an improved THM coupled mathematical model to accommodate the broadest possible suite of processes involved in GM-ECBM recovery, including governing equations of coal deformation, mass transport of ternary gases and water mixtures, and heat transfer – together with the coupling terms modulating matrix and fracture porosities and permeability.

2.1. Coupling relationships between processes

2.1.1. Coupling relationships

The following assumptions are adopted for the model [7,32,39,48,49]:

(i) The coal seam is considered as an elastic single-permeability and dual-porosity (fractures and matrix pores) material;
(ii) Ternary gases (CH_4, CO_2, and N_2) are adsorbed on the inner surface of matrix pores, while both free gases and water exist and migrate in fractures;
(iii) The free gases conform to the ideal gas law;
(iv) The fractures are saturated by the ternary gases and water mixtures; and
(v) The mass transport of ternary gases in coal seam are treated as three steps in tandem: CH_4 first desorbs from the inner surface of matrix pores satisfying the modified Langmuir equation, then diffuses from the pores to the fractures satisfying Fick's law. Finally, gas flow occurs within the fractures towards the production well satisfying Darcy's law. Transport of the injected CO_2 and N_2 occurs

Table 1
Main couplings included in current models.

Considered by	Key factors				
	Coal deformation	Two phase flow	Heat transfer and non-isothermal adsorption	Mass transport between matrix and fractures	Ternary (binary) gases competitive sorption
Durucan and Shi (2009) [24]	√	√			√
Zhu et al. (2011) [41]	√		√		
Wu et al. (2011) [39]	√			√	√
Sun et al. (2016) [37]	√	√		√	√
Sayyafzadeh et al. (2016) [46]	√	√			√
Ren et al. (2017) [40]	√			√	√
Ma et al. (2017) [44]	√	√			√
Teng et al. (2018) [43]	√		√		
Fan et al. (2018) [45]	√		√	√	√

Note: check mark identify that the process is considered in the developed model.

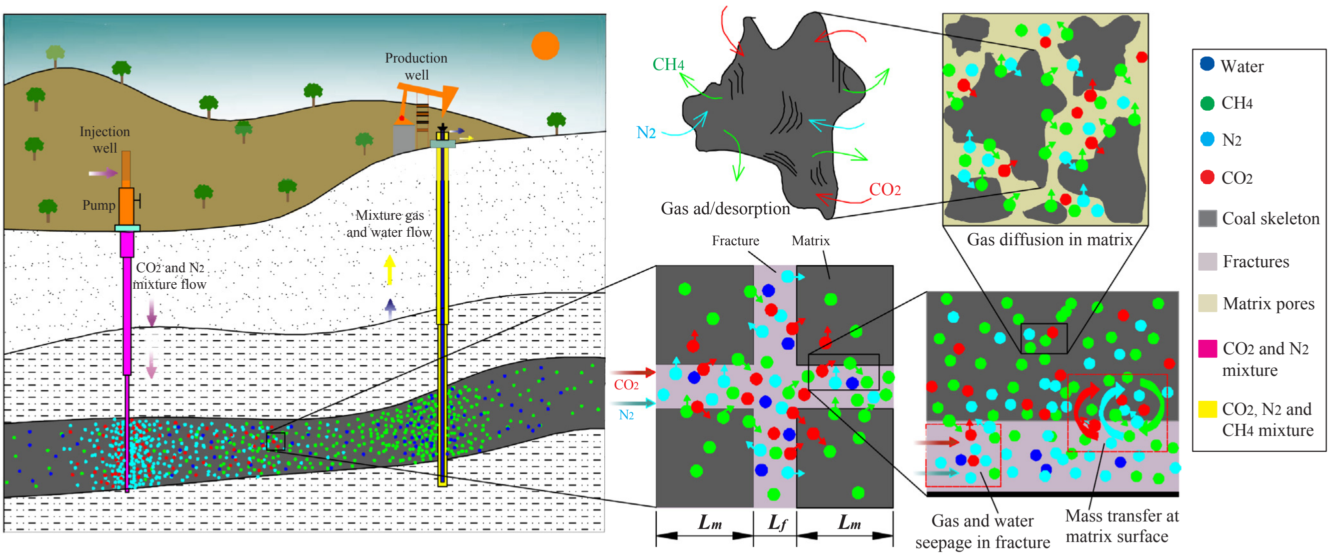

Fig. 1. Mass (CH_4, CO_2, N_2 and water) transport during GM-ECBM recovery (modified after Shi et al. (2008) [11]).

in the opposite sequence – this gas mixture first flows from the injection well to the fractures, then diffuses from the fractures to the matrix, followed by the competitive adsorption with CH_4 present on pore surfaces.

The mass transport process of gas and water mixture during GM-ECBM recovery is shown in Fig. 1. According to the aforementioned assumptions, the production and injection behaviors of GM-ECBM recovery are controlled by the coupling responses among hydraulic, thermal and mechanical fields (Fig. 2). The hydraulic field relates to the competitive non-isothermal adsorption of ternary gases (CO_2, N_2 and CH_4) in the coal matrix, gas diffusion between matrix and fractures, and the mass transport of the mixture by gas-water two-phase flow in the fractures. Competitive adsorption, gas diffusion and two-phase flow are affected not only by the corresponding partial gas pressure within the hydraulic field, but also by the thermal and mechanical fields – due to changes in porosity and permeability resulting from the varying of temperature and effective stress. In coal seams saturated with formation water, gas migration in the fractures is hindered by the low gas relative permeability, especially during the initial dewatering stage when the water saturation is relatively high. The thermal field includes heat transfer among the solid-liquid-gas phases and the energy changes induced by gas ad/desorption and coal deformation. The fluid composition and the flow rate of ternary gases and water mixture will affect the heat conduction/convection of the entire coal seam, as well as the heat transfer efficiency.

In addition, change in effective stress induced by CH_4 depletion and CO_2/N_2 injection will change the reservoir permeability, and then change the rate of heat transfer. The coal seam is characterized as a poroelastic medium with single-permeability and dual-porosity which contains both fractures and matrix pores. Gas and water are transported within the pores and fractures and in turn alter the coal deformation. Meanwhile, the thermal stress induced by changes in temperature also acts on coal skeleton to drive deformation. The following establishes a THM model for GM-ECBM recovery that considers the prior bidirectional interactions between coal deformation, heat transfer, and ternary gas mixtures and water migration.

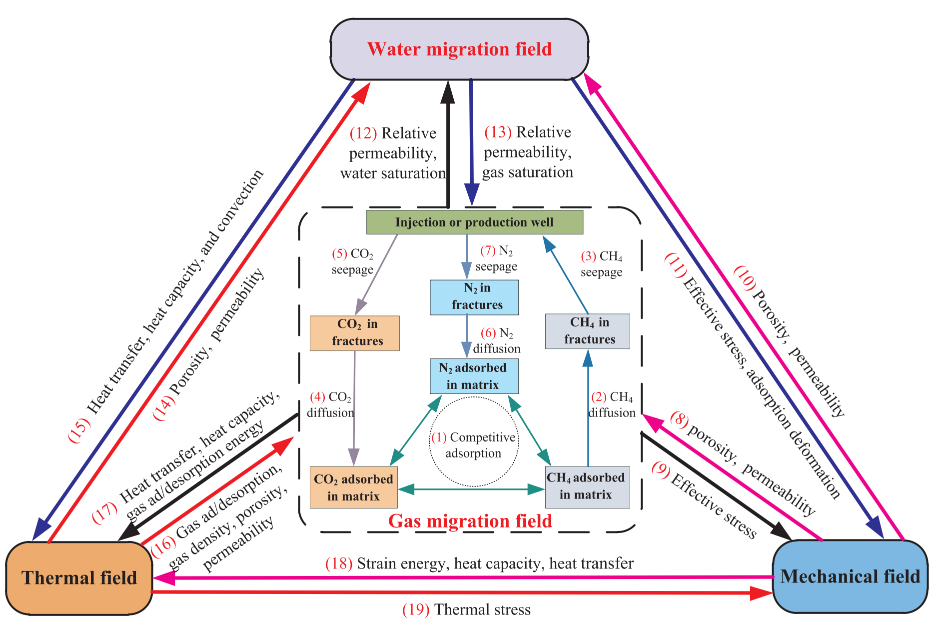

Fig. 2. Coupling relationships of the THM model for gas mixture enhanced CBM recovery.

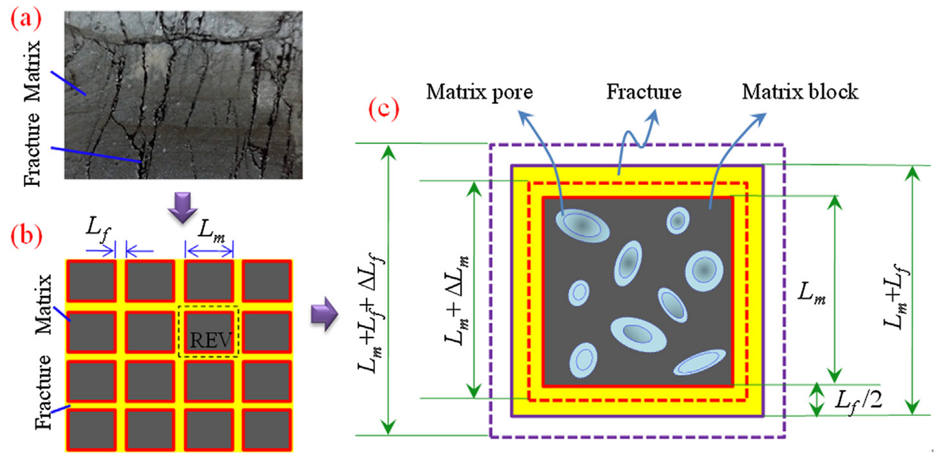

Fig. 3. Physical model of a dual-porosity and single-permeability medium: (a) actual coal surface, (b) coal structure model, (c) representative element volume (REV), where L_m is the width of the coal matrix and L_f is the facture aperture.

2.1.2. Porosity and permeability

Porosity and permeability are key factors influencing the flow of gas and water within coal seams (relations (8), (10), (14), and (16) in Fig. 2), which directly affects predictions of the evaluation of gas production and injection during GM-ECBM recovery. As shown in Fig. 3, the coal seam can be considered as a dual-porosity and single-permeability absorbing medium, which consists of fractures and coal matrix with interior pores [48,50]. Permeability is linked to fracture porosity according to the cubic law. Since fracture aperture is sensitive to the stress state and the mechanical properties of the coal seam, the permeability is concomitantly sensitive to effective stress and gas ad/desorption induced swelling/shrinkage that accompanies the process of gas production and injection.

By considering CH_4 desorption induced matrix shrinkage, CO_2 and N_2 adsorption induced matrix swelling and thermally induced coal deformation, the porosity model of matrix pores can be defined as [7]:

$$\phi_m = \phi_{m0} + \frac{(\alpha_m - \phi_{m0})(\varepsilon_e - \varepsilon_{e0})}{(1 + \varepsilon_e)} \tag{1}$$

where $\varepsilon_e = \varepsilon_v + p_m/K_s\text{-}\alpha_T T\text{-}\varepsilon_a$; ε_v is the volume strain in the coal; $\alpha_m = 1 - K/K_s$ is the Biot effective stress coefficient for the coal matrix; $K = D/3(1 - 2\nu)$ is the bulk modulus, GPa; $K_s = E_s/3(1 - 2\nu)$ is the skeleton bulk modulus, GPa; $D = 1/[1/E + 1/(L_m{\cdot}K_n)]$ is the effective elastic modulus, GPa; E is elastic modulus, GPa; K_n is the normal stiffness of the fracture, Pa/m; E_s is the skeleton elastic modulus, GPa; ν is Poisson ratio; p_m is the gas mixture pressure in matrix, MPa; α_T is thermal expansion coefficient, 1/K; T is temperature, K; T_0 is initial temperature, K; ε_a is volumetric strain of the matrix swelling/shrinkage induced by gas ad/desorption; and the subscript '0' represents the initial value of the parameter.

The ad/desorption of the ternary gases mixture on the coal matrix usually causes strain swelling/shrinkage. The volume strain induced by gas mixture sorption is the sum of strain induced by each gas component. The extended Langmuir-type equation is used with the gas sorption induced strain [39,45]:

$$\varepsilon_a = \sum_{i=1}^{3} \varepsilon_{ai} = \sum_{i=1}^{3} \frac{\varepsilon_{Li} b_{\varepsilon i} p_{mgi}}{1 + (b_{\varepsilon 1} p_{mg1} + b_{\varepsilon 2} p_{mg2} + b_{\varepsilon 3} p_{mg3})} \tag{2}$$

where ε_{Li} is the Langmuir-type strain coefficient of component i, which represents the maximum swelling capacity; $P_{\varepsilon i}$ is the Langmuir-type pressure coefficient of component i, Pa; $b_{\varepsilon i} = 1/P_{\varepsilon i}$; p_{mgi} is the gas pressure in the matrix pore of component i; and the subscript 'i' denotes of the gas component ($i = 1$ for CH_4, $i = 2$ for CO_2 and $i = 3$ for N_2).

The coal seam is a dual-porosity medium which contains both coal matrix and fractures (Fig. 3). The effective stress for the coal matrix and fracture can be defined as [51,52]:

$$\begin{cases} \sigma_{em} = \sigma - (\alpha_m p_m + \alpha_f p_f) \\ \sigma_{ef} = \sigma - \alpha_f p_f \end{cases} \tag{3}$$

where $\sigma = (\sigma_{11} + \sigma_{22} + \sigma_{33})/3$ is the average principal stress, Pa; $\alpha_f = 1 - K/(L_m{\cdot}K_n)$ is the Biot coefficient for the fractures; $p_f = s_w p_{fw} + s_g p_{fg}$ is the fluid pressure in the fracture, Pa; p_{fg} is the gas pressure in the fracture, Pa; $p_{fw} = p_{fg} - p_{cgw}$ is the water pressure in the fracture, Pa; p_{cgw} is the capillary pressure, Pa; s_w is the water saturation in the fracture; and $s_g = 1 - s_w$ is gas saturation in the fracture.

The volumetric strain of the REV can be expressed as [50]:

$$\Delta\varepsilon_v = \frac{L_m^3}{L_t^3 K_m}\Delta\sigma_{em} + \frac{L_t^3 - L_m^3}{L_t^3 K_f}\Delta\sigma_{ef} - \frac{L_m^3}{L_t^3}\Delta\varepsilon_a - \frac{L_m^3}{L_t^3}\alpha_T \Delta T \tag{4}$$

where $L_t = L_m + L_f$ is the total width of the representative elementary volume (REV), m; and K_m is the bulk modulus of the matrix, Pa.

Substituting Eq. (3) into Eq. (4), we can obtain:

$$\Delta\varepsilon_v = \frac{L_m^3}{L_t^3}\left(\frac{1}{K_m}\Delta(\sigma - (\alpha_m p_m + \alpha_f p_f)) + \frac{L_t^3 - L_m^3}{L_m^3 K_f}\Delta(\sigma - \alpha_f p_f) - \Delta\varepsilon_a - \alpha_T \Delta T\right) \tag{5}$$

The ratio $r_{mt} = L_m/L_t$ is defined as the proportion of matrix width to the REV width. Rewriting Eq. (5), the effective stress of the fracture is expressed as:

$$\Delta\sigma - \alpha_f \Delta p_f = \frac{K_m K_f}{K_f r_{mt}^3 + K_m - K_m r_{mt}^3}\left(r_{mt}^3 \Delta\varepsilon_a + r_{mt}^3 \alpha_T \Delta T + \Delta\varepsilon_v + \frac{r_{mt}^3}{K_m}\alpha_m \Delta p_m\right) \tag{6}$$

The evolution of fracture porosity is dependent on the change in effective stress-induced fracture deformation:

$$\phi_f = \phi_{f0}\left(1 + \frac{\Delta L_f}{L_f}\right) = \phi_{f0}\left(1 + \frac{1}{3K_f}(\Delta\sigma - \alpha_f \Delta p_f)\right) \tag{7}$$

where φ_{f0} is the initial fracture porosity.

Substituting Eq. (6) into Eq. (7), the fracture porosity can be obtained:

$$\phi_f = \phi_{f0} + \frac{\phi_{f0} K_m}{3(K_f + K_m/r_{mt}^3 - K_m)}\left(\Delta\varepsilon_a + \alpha_T \Delta T + \frac{\Delta\varepsilon_v}{r_{mt}^3} + \frac{\alpha_m \Delta p_m}{K_m}\right) \tag{8}$$

The cubic law is applied to define a relationship between fracture porosity and permeability:

$$k = k_0\left(\frac{\phi_f}{\phi_{f0}}\right)^3 = k_0\left(1 + \frac{K_m}{3(K_f + K_m/r_{mt}^3 - K_m)}\left(\Delta\varepsilon_a + \alpha_T\Delta T + \frac{\Delta\varepsilon_v}{r_{mt}^3} + \frac{\alpha_m\Delta p_m}{K_m}\right)\right)^3 \tag{9}$$

where k_0 is the initial permeability of the fracture, m^2.

2.2. Governing equations for hydraulic field

2.2.1. Ternary gases transport in matrix

According to Dalton's law, the pressure of a ternary mixture of non-reactive gases in matrix pores and coal fractures can be defined as [13]:

$$\begin{cases} p_m = p_{mg1} + p_{mg2} + p_{mg3} \\ p_{fg} = p_{fg1} + p_{fg2} + p_{fg3} \end{cases} \tag{10}$$

where p_{mg1}, p_{mg2}, and p_{mg3} are the gas pressure in the matrix pores for CH_4, CO_2, and N_2, respectively; and p_{fg1}, p_{fg2}, and p_{fg3} are the gas pressure in the coal fractures for CH_4, CO_2, and N_2, respectively.

The ideal gas law gives the relationship between gas pressure and density for the free ternary gases, for each component:

$$\rho_{gi} = \frac{M_{gi}}{RT}p_{gi} \tag{11}$$

where M_{gi} is the molar mass of gas component i, g/mol; p_{gi} is the gas pressure of component i, Pa; R is gas molar constant, J/(mol·K); and T is the temperature in the coal seam, K.

The gas volume adsorbed per unit mass of the coal under variable temperature can be calculated using a modified Langmuir model [41,45]:

$$V_{sgi} = \frac{V_{Li}b_{Li}p_{mgi}\exp(-c_1(T - T_{ref})/(1 + c_2p_m))}{1 + (b_{L1}p_{mg1} + b_{L2}p_{mg2} + b_{L3}p_{mg3})} \tag{12}$$

where V_{Li} is the Langmuir volume constant, m^3/kg; p_{Li} is the Langmuir pressure constant, Pa; $b_i = 1/P_{Li}$; p_{mgi} is the gas pressure in the matrix, Pa; T_{ref} is the reference temperature for the measurement of sorption, K; c_1 and c_2 are the temperature coefficient and pressure coefficient for non-isothermal adsorption.

Ternary gas transport in the coal matrix is a diffusion-dominated process, which is driven by the concentration gradient and obeys Fick's law. The gas exchange rate of each component can thus be expressed as [40]:

$$Q_{si} = -D_i\delta\frac{M_{gi}}{RT}(p_{mgi} - p_{fgi}) \tag{13}$$

where D_i is the diffusion coefficient of gas component i, m^2/s; and δ is the shape factor of cubic coal matrix blocks and can be obtained from [53]:

$$\delta = \frac{3\pi^2}{L_m^2} \tag{14}$$

where L_m is cleat spacing (matrix width), m.

The gas content in the coal matrix consists of both free and absorbed gas components. CH_4, N_2 and CO_2 are initially in a state of dynamic equilibrium in sorption/desorption. When the equilibrium state is broken by gas extraction or injection, the adsorbed CH_4 desorbs, and diffuses from the coal matrix to the fractures. Accordingly, the injected CO_2 and N_2 diffuse from the fractures to matrix pores, and adsorbs onto pore surface. By applying mass conservation, the gas migration in the coal matrix is formulated as:

$$\frac{\partial}{\partial t}(\phi_m\rho_{mgi} + V_{sgi}\rho_c\rho_{gsi}) = Q_{si} \tag{15}$$

where ρ_c is the density of coal skeleton, kg/m^3; ρ_{gsi} is the density of gas component i, kg/m^3; t is the time, s.

The desorption time τ_i is defined as the time taken for the matrix to desorb 63.2% of the total adsorbed gas, which reflects the ability for diffusion of gas between matrix pores and coal fractures, and can be expressed as [40]:

$$\tau_i = \frac{1}{D_i\delta} \tag{16}$$

Substituting Eqs. (11)–(13) and (16) into Eq. (15), the governing equation for mass transport for each component in the coal matrix can be defined as:

$$\frac{\partial}{\partial t}\left(\phi_m\frac{M_{gi}}{RT}p_{mgi} + \frac{V_{Li}b_{Li}p_{mgi}}{1 + \sum_{j=1}^{3} b_{Lj}p_{mgj}}\exp\left(\frac{-c_1(T - T_{ref})}{(1 + c_2p_m)}\right)\rho_c\rho_{gsi}\right) = -\frac{1}{\tau_i}\frac{M_{gi}}{RT}(p_{mgi} - p_{fgi}) \tag{17}$$

2.2.2. Ternary gases transport in fracture

In the coal reservoir, the pre-existing CH_4 and water and injected CO_2 and N_2 coexist and migrate within fractures. For gas migration in the fractures, CH_4 desorption from the matrix provides a mass source, while the adsorption of CO_2 and N_2 in matrix acts as a mass sink. The gas and water mixture transported as a two-phase flow, and mass conservation for gas migration in the fractures, is defined as [44,49]:

$$\frac{\partial(s_g\phi_f\rho_{fgi})}{\partial t} + \nabla\cdot(\rho_{fgi}\vec{q}_{gi}) = \frac{1}{\tau_i}\frac{M_{gi}}{RT}(p_{mgi} - p_{fgi}) \tag{18}$$

where s_g is the gas saturation in the fracture; ρ_{fgi} is the density of gas component i, kg/m^3; and q_{gi} is the velocity of gas component i, m/s.

By considering the Klinkenberg effect within the porous medium and gas-water two-phase flow, the velocity of gas flow in the fracture can be defined by the Darcy's law as [7]:

$$\vec{q}_{gi} = -\frac{kk_{rg}}{\mu_{gi}}\left(1 + \frac{b_k}{p_{fgi}}\right)\nabla p_{fgi} \tag{19}$$

where k is the absolute permeability of the coal seam, which is defined by Eq. (9), m^2; k_{rg} is the gas relative permeability; μ_{gi} is the dynamic viscosity of gas component i, Pa·s; and b_k is the Klinkenberg factor, Pa.

The relative permeability curves in the porous medium are often expressed with the Corey functions [54]. The relative permeabilities for gas and water phases are defined as [55]:

$$\begin{cases} k_{rg} = k_{rg0}(1 - s_e)^\eta\left(1 - (s_e)^{1+\frac{2}{\lambda}}\right) \\ k_{rw} = k_{rw0}(s_e)^{\eta+1+\frac{2}{\lambda}} \end{cases} \tag{20}$$

where k_{rg0} is the endpoint relative permeability of the gas, k_{rw0} is the endpoint relative permeability of water; λ is the cleat size distribution index; η is the tortuosity coefficient for the relative permeability; and s_e is the effective water saturation, defined as [7,56]:

$$s_e = \frac{s_w - s_{wr}}{1 - s_{wr} - s_{gr}} \tag{21}$$

where s_{wr} is the irreducible water saturation; s_{gr} is the residual gas saturation. The capillary pressure is also related to the effective saturation [55]:

$$p_{cgw} = p_e(s_e)^{-1/\lambda} \tag{22}$$

where p_e is the entry pressure, Pa.

Substituting Eqs. (19) and (20) into Eq. (18), the governing equations for transport of the ternary gas mixture in the fractures can be obtained as:

$$\frac{\partial}{\partial t}(s_g\phi_f p_{fgi}) + \nabla\cdot\left(-\frac{kk_{rg0}p_{fgi}}{\mu_{gi}}(1-s_e)^{\eta}\left(1-(s_e)^{1+\frac{2}{\lambda}}\right)\left(1+\frac{b_k}{p_{fgi}}\right)\nabla p_{fgi}\right) = \frac{1}{\tau_i}(p_{mgi}-p_{fgi}) \quad (23)$$

2.2.3. Water transport in fracture

Absent a source term, the coal reservoir gradually dewaters with the progress of gas injection and production. For two-phase flow and mass conservation, the equation for water transport in the fractures is defined as [49]:

$$\frac{\partial(s_w\phi_f\rho_w)}{\partial t} + \nabla\cdot(\rho_w\vec{q}_w) = 0 \quad (24)$$

where s_w is the water saturation; p_{fw} is the water pressure in the fractures, Pa; ρ_w is water density, kg/m^3.

Also, the velocity of water can be expressed by the Darcy's law as:

$$\vec{q}_w = -\frac{kk_{rw}}{\mu_w}\nabla p_{fw} \quad (25)$$

where k_{rw} is the water relative permeability; and μ_w is the dynamic viscosity of water, Pa·s.

By substituting Eqs. (20) and (25) into Eq. (24), we obtain the governing equation of water transport in the fracture as:

$$\frac{\partial(s_w\phi_f\rho_w)}{\partial t} + \nabla\cdot\left(-\frac{\rho_w kk_{rw0}}{\mu_w}(s_e)^{\eta+1+\frac{2}{\lambda}}\nabla p_{fw}\right) = 0 \quad (26)$$

2.3. Governing equations for coal deformation

The deformation induced by the pressure of fluid mixture in both matrix and fractures (effective stress), together with shrinkage/swelling induced by gas sorption/desorption and thermal effects defines the total strain as [39,40,43]:

$$\varepsilon_{kl} = \frac{1}{2G}\sigma_{kl} - \left(\frac{1}{6G}-\frac{1}{9K}\right)\sigma_{dd}\delta_{kl} + \frac{\alpha_m p_m + \alpha_f p_f}{3K}\delta_{kl} + \frac{\alpha_T T}{3}\delta_{kl} + \frac{\varepsilon_a}{3}\delta_{kl} \quad (27)$$

where $G = D/2(1+\nu)$ is the bulk modulus, Pa; ν is Poisson ratio; $D = 1/[1/E + 1/(L_m K_n)]$ is the effective elastic modulus, Pa; K_n is the normal stiffness of the fracture, Pa/m; E is the elastic modulus, Pa; $K = D/3(1-2\nu)$ is bulk modulus, Pa; and δ_{kl} is the Kronecker delta with 1 for $k = l$ and 0 for $k \neq l$.

The strain-displacement relation (the Cauchy formula) and stress equilibrium relations can be expressed as [7]:

$$\begin{cases} \varepsilon_{kl} = \frac{1}{2}(u_{k,l}+u_{l,k}) \\ \sigma_{kl,l} + f_k = 0 \end{cases} \quad (28)$$

where u_k is the deformation in the k direction, m; f_k is the body force in the k direction, N; k, l = x, y, z.

Substituting Eq. (28) into Eq. (27), the governing equation for mechanical field can be obtained:

$$Gu_{k,ll} + \frac{G}{1-2\upsilon}u_{l,lk} - (\alpha_m p_{m,k} + \alpha_f p_{f,k}) - K\alpha_T T_{,k} - K\left(\sum_{i=1}^{3}\frac{\varepsilon_{Li}b_{\varepsilon i}p_{mgi}}{1+\sum b_{\varepsilon j}p_{mgj}}\right)_{,k} + f_k = 0 \quad (29)$$

2.4. Governing equations for heat transfer

The coal skeleton, ternary gas mixture and water are contained within a single representative elementary volume (REV). When the gas mixture is injected into the coal seam, heat transfer occurs due to the variation in internal energy caused by temperature change, strain energy by coal deformation, isosteric heat by gas de/adsorption, as well as the heat convection and conduction among the solid-gas-water phases. The thermal equilibrium within the REV is may be expressed as [7,41,45]:

$$\frac{\partial}{\partial t}((\rho C_p)_{eff}T) + \eta_{eff}\nabla T - \nabla\cdot(\lambda_{eff}\nabla T) + K\alpha_T T\frac{\partial\varepsilon_v}{\partial t} + \sum_{i=1}^{3}q_{sti}\frac{\rho_s\rho_{gsi}}{M_{gi}}\frac{\partial V_{sgi}}{\partial t} = 0 \quad (30)$$

where $(\rho C_p)_{eff}$ is the effective specific heat capacity of coal mass, J/(m^3·K); η_{eff} is the effective heat convection coefficient of the fluid mixture, J/(m^2·s); λ_{eff} is the effective thermal conductivity, W/(m·K); q_{sti} is the isosteric heat of gas adsorption of component i, kJ/mol. In Eq. (30), the terms from left to right represent, respectively, the change of internal energy, heat convection, heat conduction, strain energy of the coal skeleton and gas de/adsorption heat.

The effective specific heat capacity is determined by the density and the specific heat capacity of all components within the coal mass:

$$(\rho C_p)_{eff} = (1-\phi_f-\phi_m)\rho_s C_s + \sum_{i=1}^{3}(s_g\phi_f\rho_{fgi} + \phi_m\rho_{mgi})C_{gi} + s_w\phi_f\rho_w C_w \quad (31)$$

where C_s, C_{gi} and C_w, are the specific heat capacities of the coal skeleton, ternary gas (CH_4, CO_2, and N_2) and water, respectively, J/(kg·K).

The effective heat convection coefficient of the coal mass is related to the convective heat transfer of the gas and water mixture in the fracture:

$$\eta_{eff} = -\sum_{i=1}^{3}\left(\frac{\rho_{fgi}C_{gi}kk_{rg}}{\mu_{gi}}\left(1+\frac{b_{ki}}{p_{fgi}}\right)\nabla p_{fgi}\right) - \frac{\rho_w C_w kk_{rw}}{\mu_w}\nabla p_{fw} \quad (32)$$

The effective thermal conductivity of the coal mass is a linear combination of the thermal conductivity of each component:

$$\lambda_{eff} = (1-\phi_f-\phi_m)\lambda_s + \phi_m\lambda_{mg} + \phi_f(s_g\lambda_{fg} + s_w\lambda_{fw}) \quad (33)$$

where λ_s, λ_{mg}, λ_{fg} and λ_{fw} are the thermal conduction coefficients for the coal skeleton, gas mixture in the matrix, gas mixture in the fracture, and water in the fracture, respectively, W/(m·K).

We assemble the governing equations representing the different fields (Eqs. (17), (23), (26), (29) and (30)), together with the coupling terms of Eqs. (1), (8) and (9), to establish the fully coupled thermo-hydro-mechanical model for GM-ECBM recovery.

$$\begin{cases} \frac{\partial}{\partial t}\left(\phi_m\frac{M_{gi}}{RT}p_{mgi} + \frac{V_{Li}b_{Li}p_{mgi}}{1+\sum_{j=1}^{3}b_{Lj}p_{mgj}}\exp\left(\frac{-c_1(T-T_{ref})}{(1+c_2p_m)}\right)\rho_c\rho_{gsi}\right) = -\frac{1}{\tau_i}\frac{M_{gi}}{RT}(p_{mgi}-p_{fgi}) \\ \frac{\partial}{\partial t}(s_g\phi_f p_{fgi}) + \nabla\cdot\left(-\frac{kk_{rg0}p_{fgi}}{\mu_{gi}}(1-s_e)^{\eta}\left(1-(s_e)^{1+\frac{2}{\lambda}}\right)\left(1+\frac{b_k}{p_{fgi}}\right)\nabla p_{fgi}\right) = \frac{1}{\tau_i}(p_{mgi}-p_{fgi}) \\ \frac{\partial(s_w\phi_f\rho_w)}{\partial t} + \nabla\cdot\left(-\frac{\rho_w kk_{rw0}}{\mu_w}(s_e)^{\eta+1+\frac{2}{\lambda}}\nabla p_{fw}\right) = 0 \\ Gu_{k,ll} + \frac{G}{1-2\upsilon}u_{l,lk} - (\alpha_m p_{m,k} + \alpha_f p_{f,k}) - K\alpha_T T_{,k} - K\left(\sum_{i=1}^{3}\frac{\varepsilon_{Li}b_{\varepsilon i}p_{mgi}}{1+\sum b_{\varepsilon j}p_{mgj}}\right)_{,k} + f_k = 0 \\ \frac{\partial}{\partial t}((\rho C_p)_{eff}T) + \eta_{eff}\nabla T - \nabla\cdot(\lambda_{eff}\nabla T) + K\alpha_T T\frac{\partial\varepsilon_v}{\partial t} + \sum_{i=1}^{3}q_{sti}\frac{\rho_s\rho_{gsi}}{M_{gi}}\frac{\partial V_{sgi}}{\partial t} = 0 \end{cases} \quad (34)$$

where subscript "i" denotes gas component ($i = 1$ for CH_4, $i = 2$ for CO_2, $i = 3$ for N_2), and,

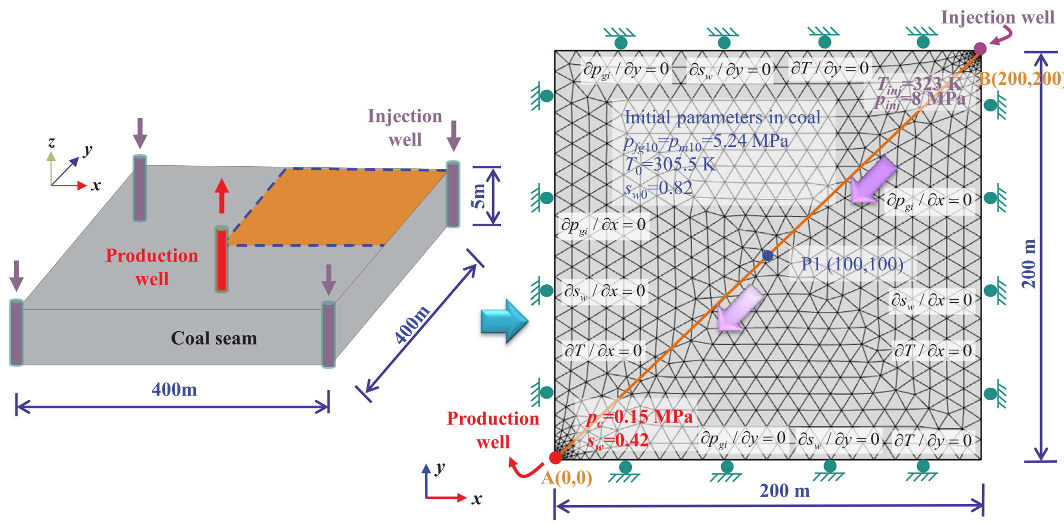

Fig. 4. Geometry and defined condition for model validation and GM-ECBM recovery.

$$\begin{cases} \phi_m = \phi_{m0} + \frac{(\alpha_m - \phi_{m0})(\varepsilon_e - \varepsilon_{e0})}{(1+\varepsilon_e)} \\ \phi_f = \phi_{f0} + \frac{\phi_{f0} K_m}{3(K_f + K_m / r_{mt}^3 - K_m)} \left(\Delta\varepsilon_a + \alpha_T \Delta T + \frac{\Delta\varepsilon_v}{r_{mt}^3} + \frac{\alpha_m \Delta p_m}{K_m} \right) \\ k = k_0 \left(\frac{\phi_f}{\phi_{f0}} \right)^3 \\ \quad = k_0 \left(1 + \frac{K_m}{3(K_f + K_m / r_{mt}^3 - K_m)} \left(\Delta\varepsilon_a + \alpha_T \Delta T + \frac{\Delta\varepsilon_v}{r_{mt}^3} + \frac{\alpha_m \Delta p_m}{K_m} \right) \right)^3 \end{cases}$$

This model comprises of a series of partial differential equations (PDEs), which can be implemented into COMSOL multiphysics software using the pre-arranged geomechanics module together with eight general form PDE interfaces to obtain numerical solution.

2.5. Simplified THM model for primary CBM recovery

Primary CBM recovery involves the transport of a single gas phase and water in the coal seam. In order to compare the gas production efficiency between primary and enhanced CBM recoveries, a model of single gas transport is required. Here, we simplify the already established THM model Eq. (34) by neglecting the roles of p_{m2}, p_{f2}, p_{m3} and p_{f3}. This results in the following model:

$$\begin{cases} \frac{\partial}{\partial t}\left(\phi_m \frac{M_{g1}}{RT} p_{mg1} + \frac{V_{L1} b_{L1} p_{mg1}}{1 + b_{L1} p_{mg1}} \exp\left(\frac{-c_1 (T - T_{ref})}{(1 + c_2 p_m)} \right) \rho_c \rho_{gs1} \right) = -\frac{1}{\tau_1} \frac{M_{g1}}{RT} (p_{mg1} - p_{fg1}) \\ \frac{\partial}{\partial t}(s_g \phi_f p_{fg1}) + \nabla \cdot \left(-\frac{k k_{rg0} p_{fg1}}{\mu_{g1}} (1 - s_e)^\eta \left(1 - (s_e)^{1 + \frac{2}{\lambda}} \right) \left(1 + \frac{b_k}{p_{fg1}} \right) \nabla p_{fg1} \right) \\ \quad = \frac{1}{\tau_1}(p_{mg1} - p_{fg1}) \\ \frac{\partial (s_w \phi_f \rho_w)}{\partial t} + \nabla \cdot \left(-\frac{\rho_w k k_{rw0}}{\mu_w} (s_e)^{\eta + 1 + \frac{2}{\lambda}} \nabla p_{fw} \right) = 0 \\ G u_{k,ll} + \frac{G}{1 - 2v} u_{l,lk} - (\alpha_m p_{m,k} + \alpha_f p_{f,k}) - K \alpha_T T_{,k} - K \left(\frac{\varepsilon_{L1} b_{\varepsilon 1} p_{mg1}}{1 + b_{\varepsilon 1} p_{mg1}} \right)_{,k} + f_k \\ \quad = 0 \\ \frac{\partial}{\partial t}((\rho C_p)_{eff} T) + \eta_{eff} \nabla T - \nabla \cdot (\lambda_{eff} \nabla T) + K \alpha_T T \frac{\partial \varepsilon_v}{\partial t} + q_{st1} \frac{\rho_s \rho_{gs1}}{M_{g1}} \frac{\partial V_{sg1}}{\partial t} = 0 \end{cases} \tag{35}$$

The simplified THM model for primary CBM recovery, Eq. (35), also comprises the governing equations of coal deformation, mass transfer between the matrix and fractures and two-phase flow in the fracture, together with the thermal field. However, only single gas (CH_4) adsorption is considered instead of ternary (CH_4, CO_2, and N_2) co-adsorption. The transport of CO_2, and N_2 within the matrix and fractures of the coal seam is also ignored. This simplified model is defined to simulate primary CBM recovery to validate the established THM model for GM-ECBM recovery against rare data from field pilot studies.

3. Numerical modelling of gas mixture injection enhanced CBM recovery

The established THM model is first validated against primary CBM recovery *in situ*, and then applied to simulate the process of GM-ECBM recovery. The evolutions of significant parameters including gas pressure, gas content, reservoir temperature, permeability, CH_4 production, CO_2 and N_2 storage are comprehensively analyzed.

3.1. Reservoir conditions and numerical model

3.1.1. Objective and model geometry

The Fanzhuang area represents a typical block for CBM development in Qinshui Basin – one of the earliest developed and most commercially valuable basins in China. Coal seam #3 is characterized by uniform thickness, high gas content and shallow burial depth and is considered as the primary target for CBM recovery from the Shanxi formation [57]. The pressure depletion method is generally adopted for coalbed methane recovery [37]. However, with the decrease of reservoir pressure, gas production rate decreases rapidly, motivating the numerical investigation of gas injection enhanced CBM recovery to maximize both methane recovery and CO_2 sequestration.

Two sets of simulations are performed in this section: (i) the first is to validate the established THM model through history matching with *in situ* observations of natural pressure depletion in an unstimulated production well; (ii) the second is to apply the validated model to simulate the process of GM-ECBM recovery, together with the evolution of key parameters.

Well spacing varies from 334.67 m to 537.98 m, with shallow vertical CBM wells usually arranged on a rectangle pattern of 300 m × 300 m–500 m × 500 m[7]. Here, an intermediate well pattern of 400 m × 400 m is adopted, as shown in Fig. 4. The production well is located at the center of domain surrounding by four injection wells. Because of the repeating symmetry of the geometric model, we use a quadrant located in the upper right corner of the geometry for the numerical simulation. For GM-ECBM recovery, a production well and an injection well are designed at the lower left corner and the upper right corner of this 2D geometry. While for primary CBM recovery, only a production well is set to the lower left corner. The section A-B and point P1 in the 2D geometry are set to measure the variation of reservoir parameters.

Table 2
Related parameters for the simulation of GM-ECBM recovery.

Parameter	Value	Remark	Parameter	Value	Remark
Initial CH_4 pressure in fracture (p_{fg10}, MPa)	5.24	Field data	Initial CH_4 pressure in matrix (p_{mg10}, MPa)	5.24	Field data
Initial CO_2 pressure in fracture (p_{fg20}, MPa)	0.1	Estimation	Initial CO_2 pressure in matrix (p_{mg20}, MPa)	0.1	Estimation
Initial N_2 pressure in fracture (p_{fg30}, MPa)	0.1	Estimation	Initial N_2 pressure in fracture (p_{fg30}, MPa)	0.1	Estimation
Langmuir volume constant of CH_4 (V_{L1}, m^3/kg)	0.0196	Experiments	Langmuir pressure constant of CH_4 (P_{L1}, MPa)	1.32	Experiments
Langmuir volume constant of CO_2 (V_{L2}, m^3/kg)	0.0304	Experiments	Langmuir pressure constant of CO_2 (P_{L2}, MPa)	0.83	Experiments
Langmuir volume constant of N_2 (V_{L3}, m^3/kg)	0.0146	Experiments	Langmuir pressure constant of N_2 (P_{L3}, MPa)	2.61	Experiments
Langmuir strain constant of CH_4 (ε_{L1})	0.0128	[25]	Adsorption time of CH_4 (τ_1, d)	4.34	[40]
Langmuir strain constant of CO_2 (ε_{L2})	0.0362	[25]	Adsorption time of CO_2 (τ_2, d)	4.34	[40]
Langmuir strain constant of N_2 (ε_{L3})	0.0058	[25]	Adsorption time of N_2 (τ_2, d)	4.34	[40]
Dynamic viscosity of CH_4 (μ_1, Pa·s)	1.03×10^{-5}	[58]	Temperature coefficient (c_1, 1/T)	0.02	[41]
Dynamic viscosity of CO_2 (μ_2, Pa·s)	1.37×10^{-5}	[58]	Pressure coefficient (c_2, 1/MPa)	0.07	[41]
Dynamic viscosity of N_2 (μ_3, Pa·s)	1.70×10^{-5}	[58]	Isosteric heat of CH_4 adsorption (q_{st1}, kJ/mol)	15.3	Estimation
Dynamic viscosity of water (μ_w, Pa·s)	1.01×10^{-3}	[58]	Isosteric heat of CO_2 adsorption (q_{st2}, kJ/mol)	19.2	Estimation
Thermal conductivity of CH_4 (λ_{g1}, W/(m·K))	0.0371	[58]	Isosteric heat of N_2 adsorption (q_{st3}, kJ/mol)	12.8	Estimation
Thermal conductivity of CO_2 (λ_{g2}, W/(m·K))	0.0168	[58]	Initial water saturation (s_{wi})	0.82	Field data
Thermal conductivity of N_2 (λ_{g3}, W/(m·K))	0.0262	[58]	Irreducible water saturation (s_{wr})	0.32	Estimation
Thermal conductivity of water (λ_w, W/(m·K))	0.5985	[58]	Residual gas saturation (s_{gr})	0.15	Estimation
Thermal conductivity of coal (λ_s, W/(m·K))	0.1913	[7]	Klinkenberg factor (b_k, MPa)	0.36	Experiments
Specific heat capacity of CH_4 (C_{g1}, J/(kg·K))	2 160	[7]	Entry capillary pressure (p_e, MPa)	0.1	[44]
Specific heat capacity of CO_2 (C_{g2}, J/(kg·K))	844	[58]	Cleat size distribution index (λ)	1.2	[59]
Specific heat capacity of N_2 (C_{g3}, J/(kg·K))	1040	[58]	Tortuosity coefficient (η)	1	[59]
Specific heat capacity of coal (C_s, J/(kg·K))	1350	[7]	Fracture stiffness (K_n, GPa/m)	2.8	Field data
Specific heat capacity of water (C_w, J/(kg·K))	4200	[7]	Poisson's ratio of coal (ν)	0.32	Experiments
Initial permeability of fracture (k_0, mD)	0.924	Field data	Initial temperature in coal seam (T_0, K)	305.5	Field data
Porosity of matrix (φ_m)	0.0423	[39]	Coal density (ρ_c, kg/m^3)	1350	Field data
Porosity of fracture (φ_f)	0.001	[39]	Buried depth of coal seam (H, m)	600	Field data
Reference temperature for adsorption test (T_{ref}, K)	300	[7]	Young's modulus of coal seam (E, MPa)	2713	[39]
Thermal expansion coefficient of coal (α_T, 1/K)	2.4×10^{-5}	[41]	Young's modulus of skeleton (Es, MPa)	8143	[39]

3.1.2. Initial and boundary conditions

Coal seam #3 is characterized by an average thickness of 5–6 m, a relatively high permeability of 0.01–10 mD, a rich gas content of 8.27–21.54 m^3/t and an average burial depth of ~600 m [60]. In this study, the initial values of reservoir pressure, temperature, permeability and water saturation are set as 5.24 MPa, 305.5 K, 0.924 mD and 0.82 respectively. The bottom hole pressure of the production well is 0.15 MPa, and the injection pressure of the gas mixture (CO_2, N_2) is 8 MPa for GM-ECBM recovery (no gas injection for primary CBM recovery). According to the local temperature and the temperature of the gas transported in pipeline, the temperature on the wall of injection well is set to 323.15 K. Table 2 lists the parameters used in the study. These parameters are mainly recovered from field tests and laboratory experiments, as well as details recorded in the public domain (Table 2).

As shown in Fig. 4, the slip condition is applied to the domain boundaries that are also insulated for mass transport and heat transfer, except for the injection and production wells. The model comprises 1558 tetrahedral elements and 32,650 degrees of freedom with the duration of both primary and enhanced recovery extending to 6000 days (~16.5 years).

3.2. Model validation by history matching

The simulated results for primary CBM recovery are compared with the historic production data from the Qinshui Basin. Sun et al. (2016) reported the historic production rate from an unstimulated production well subject to pressure depletion recovery *in situ* [37]. Fig. 5 presents the match between measured and modeled CH_4 production rate. Compared to the field data, the simulated production rate exhibits an initial transient decrease that rapidly steepens, followed by a gradual decrease with time. Two peak production rates are typically in simulation – the first may result from the rapid release of free gas in the coal seam near the production well with the second liberated by dewatering. This phenomenon is common in Qinshui Basin during pressure depletion production [37]. Gas transport in the coal seam is the combined results of competitive sorption, water seepage, and thermal and mechanical effects. The average relative error of CH_4 production rate is ~16.3%. Despite a slight deviation in the high/low rate stage, the modelling and field results foe production rate are generally in good agreement. This illustrated that the proposed THM model can be used to simulate the primary CBM recovery, as well as extended to GM-ECBM recovery.

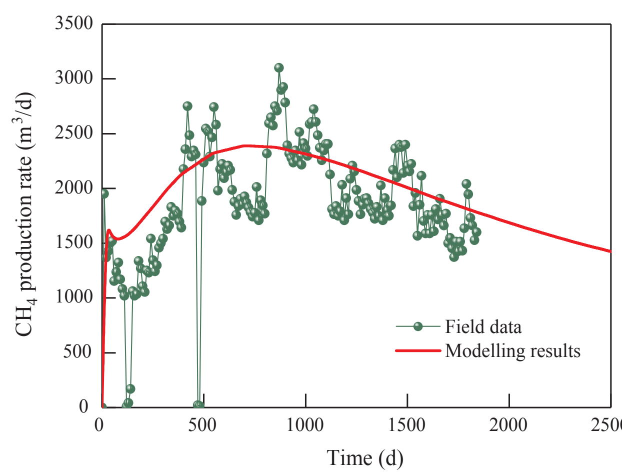

Fig. 5. History match of CH_4 production rate during primary CBM recovery.

3.3. Modelling results of GM-ECBM and primary CBM recovery

We simulate the GM-ECBM recovery using the injection gas mixture 15%:85% CO_2:N_2 (representing flue gas) and injection pressure of 8.0 MPa to track the evolutions of gas pressure, gas content, reservoir temperature, permeability, CH_4 production and CO_2, N_2 storage to provide a process-based understanding of the entire process. The gas composition and injection pressure are retained constant during the entire span of injection.

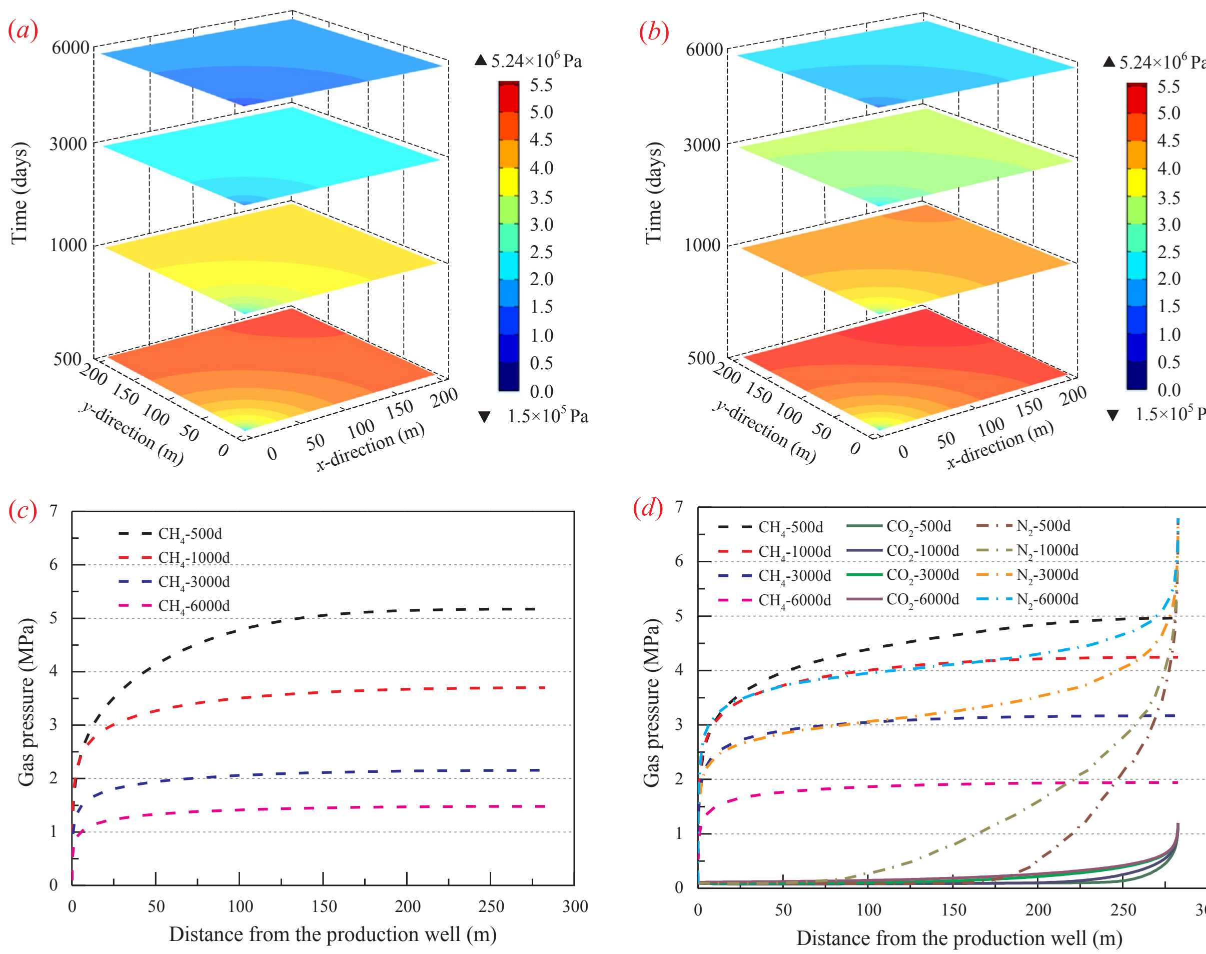

Fig. 6. Gas pressure distribution: CH_4 pressure contours for both (a) primary and (b) GM-ECBM recovery; (c) CH_4 pressure on section A-B for primary recovery; (d) CH_4, CO_2 and N_2 pressures on section A-B for GM-ECBM recovery.

3.3.1. Gas pressure evolution

Fig. 6 shows the distribution of gas pressure in the coal matrix for both primary CBM and GM-ECBM recoveries. The CH_4 pressure of both primary and enhanced recoveries gradually declines with time, with the early decline being faster than in the late stage (Fig. 6(a) and (b)). Compared to primary recovery, the CH_4 pressure during GM-ECBM recovery decreases more rapidly at early time due to the displacement effect of the injected gas mixture (CO_2, N_2), and then deceases more slowly in the later stage – this may result from the pressure compensation effect of continuous injection (Fig. 6(c) and (d)). As shown in Fig. 6(d), both CO_2 and N_2 pressures within the coal seam increase with the progress of injection.

3.3.2. Gas content evolution

Fig. 7 shows the distribution of gas content of both primary CBM and GM-ECBM recoveries. For primary recovery, the CH_4 content near the production well gradually decreases with time, with a zone of decreasing CH_4 content close to the well (Fig. 7(a)). For GM-ECBM recovery, in addition to the depleted zone around the production well, CH_4 content near the injection well also decreases over time, driven by the higher competitive adsorption capacity of CO_2 accompanying the continuous injection of gas mixture. This results in two zones of decreased CH_4 contour (Fig. 7(b)). The CH_4 content during GM-ECBM recovery decreases faster than that during primary recovery (Fig. 7(c) and (d)). For instance, CH_4 content at point P1 (100, 100) varies from 13.5 cm^3/g (500 day) to 6.4 cm^3/g (6000 days) for GM-ECBM recovery, compared to spanning from 13.4 cm^3/g to 9.2 cm^3/g for primary CBM recovery. Due to the sweeping-effect of the injected gases, CH_4 near the injection well is driven towards the production well, leading to enhanced CH_4 content during GM-ECBM at point P1 relative to primary production of CBM. In Fig. 7(d), CO_2 and N_2 contents increase with the continuous injection. Since N_2 has a lower dynamic viscosity and weaker adsorption capacity, N_2 transport faster than CO_2 in the coal seam. Hence, the N_2 content at any specific point in coal seam increases earlier than does CO_2 content.

3.3.3. Reservoir temperature evolution

Fig. 8 shows the variation of reservoir temperature at different production times. As gas pressure drops due to production, CH_4 desorption-induced heat dissipation increases, resulting in a continuous decrease in reservoir temperature during primary recovery (Fig. 8(a)). This phenomenon is increasingly more apparently near the production well. For instance, the reservoir temperature at reference point P1 varies from 305.2 K (500 d) to 303.1 K (6000 d). Gas injection at an elevated temperature results in an apparent rise in reservoir temperature near the injection well (305.5 K to 323.5 K), as shown in Fig. 8(b).

However, due to the large volume and thermal mass of coal *in situ*, the migration rate of the apparent temperature-rise front is restricted, resulting in a limited extend of this elevated temperature zone. The sweep of N_2 flow accelerates CH_4 desorption and subsequent transport, and hence promotes a decrease in reservoir temperatures distant from the injection well even prior to the arrival of CO_2.

3.3.4. Reservoir permeability evolution

As demonstrated in Eq. (9), effective reservoir permeability is the competitive result of effects driven by changes in effective stress, gas

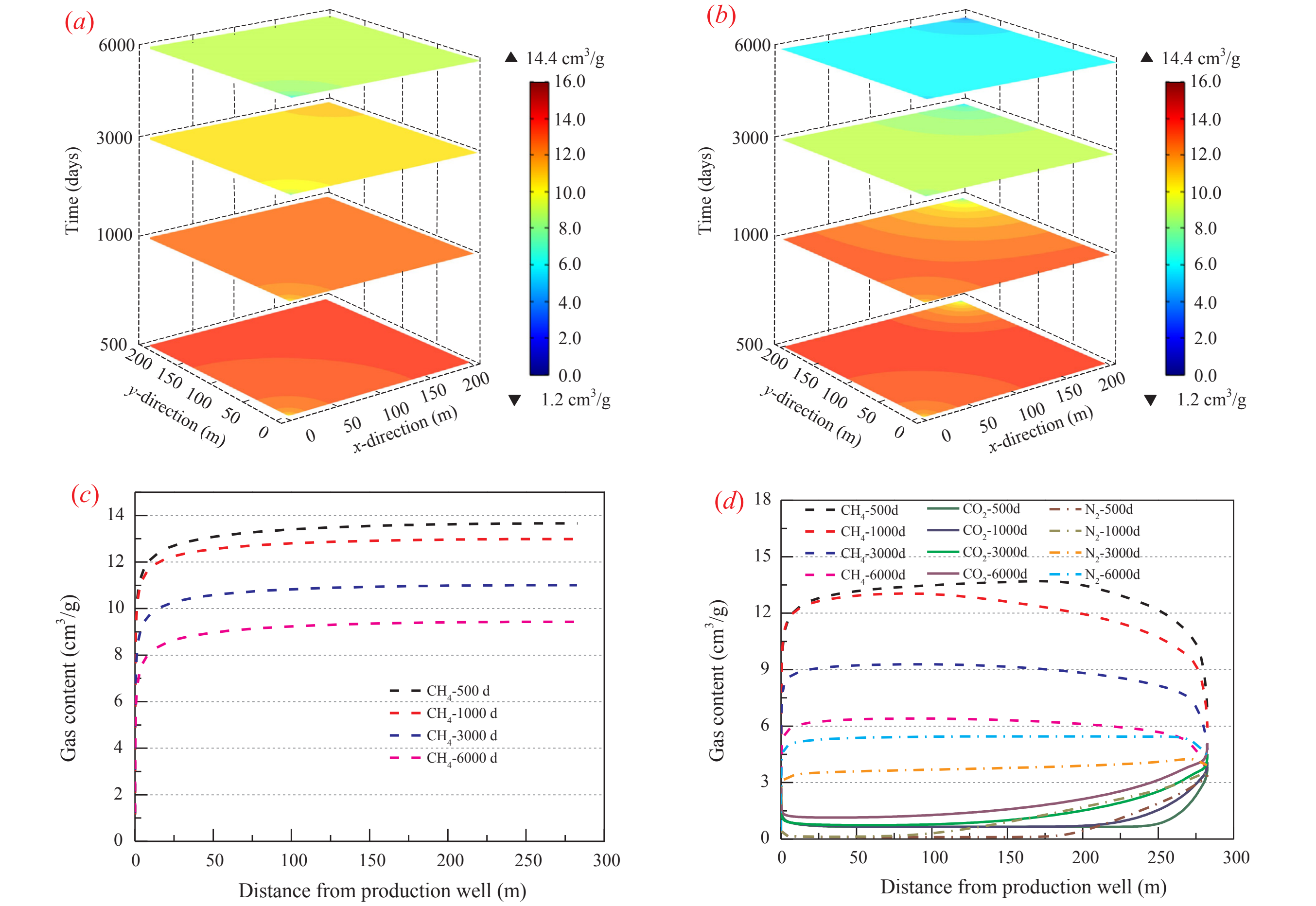

Fig. 7. Gas content distribution: CH_4 content contours for both (a) and (b) primary and GM-ECBM recoveries; (c) CH_4 content on section A-B for primary recovery; (d) CH_4, CO_2 and N_2 content on section A-B for GM-ECBM recovery.

ad/desorption induced swelling/shrinkage and thermal deformation.

Fig. 9(a) presents the evolution of reservoir permeability due to primary CBM recovery. Compared to the small decline in temperature and minor increase in effective stress, CH_4 desorption induced shrinkage dominates the evolution of permeability, leading to an increase in permeability, especially near the production well. As production time progresses, permeability ratio rises within the entire coal reservoir – increasing from ~0.997 (500 d) to ~1.132 (6000 d) at point P1.

Fig. 9(b) shows reservoir permeability along section A-B for GM-ECBM recovery and resulting from the influence of both gas mixture injection and CH_4 production. Before the arrival of the injected gas, permeability is dominated by the impact of desorption-induced shrinkage. Hence, permeability close to the production well has a rapid increase. The displacement effect of injected gas mixture occurs near the injection well. The N_2 flow with elevated N_2 concentration travels

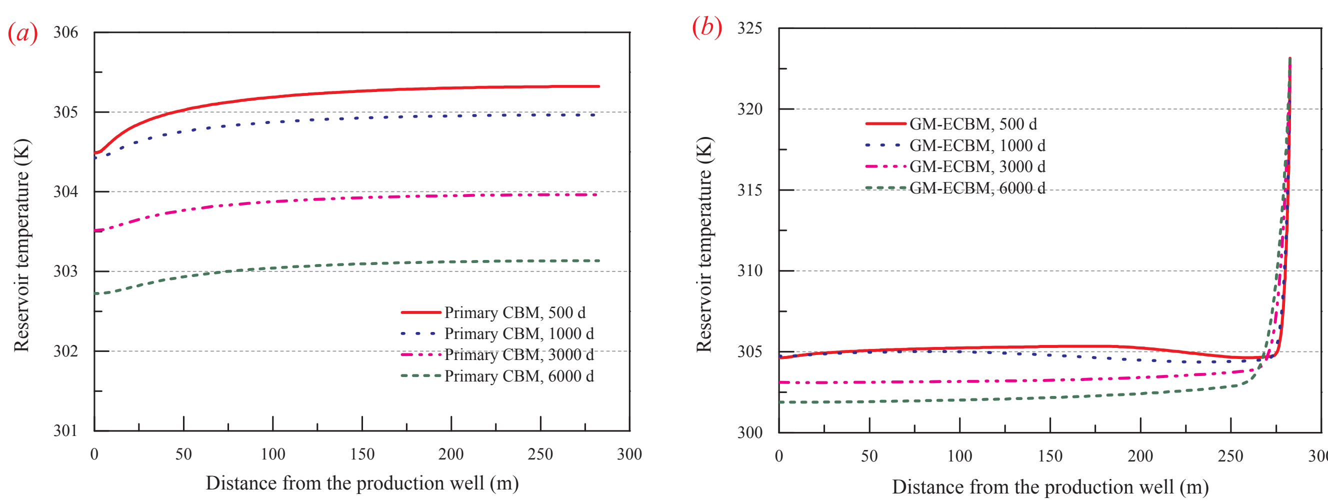

Fig. 8. Reservoir temperature on section A-B: (a) primary CBM recovery and (b) GM-ECBM recovery.

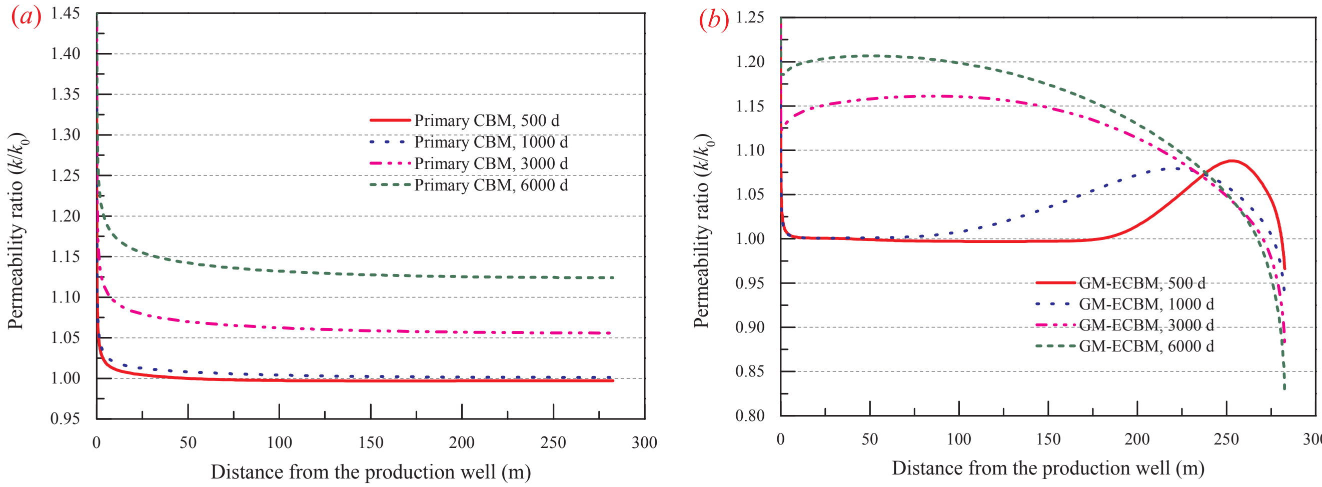

Fig. 9. Reservoir permeability on section A-B: (a) primary CBM recovery and (b) GM-ECBM recovery.

in advance of the CO_2, causing a feedback with increased CH_4 desorption and then transport towards the production well – this results in a faster early stage increase in permeability, as apparent in the permeability ration curve at 500 d and 1000 d (Fig. 9 (b)). CO_2 is retarded and travels slower, relative to N_2, but it has greater competitive adsorption capacity thus larger swelling effect when adsorbed on the coal matrix. Thus, CO_2 will play a leading role at the location of arrival. For example, permeability ratio declines dramatically near the injection well, from 0.966 (500 d) to 0.823 (6000 d).

3.3.5. Gas production and storage evolution

Fig. 10 presents the variation of CH_4 production and CO_2, N_2 storage. The CH_4 production rate of both primary and GM-ECBM recoveries first decline slightly, then climb to a peak value, before continuously declining to a residual magnitude (Fig. 10(a)). The peak production rates of primary and GM-ECBM recoveries are ~2424 and ~2958 m^3/d, respectively, appearing at ~680 and ~1540 d. This reveals that GM-ECBM recovery usually has an elevated but delayed CH_4 production peak. For GM-ECBM recovery (15%CO_2/85%N_2), the rapid transport of N_2 delivers a significant mass of N_2 injection and an early breakthrough. However, the slow migration limits the injection of CO_2, which has a low peak injection rate and a late breakthrough. Apparent from Fig. 10(b), the cumulative gas production/storage of both primary and GM-ECBM recoveries increases with time. The injected gas mixture significantly enhances the production of CH_4. Taking 6000 days of production as a reference, the cumulative CH_4 production of primary recovery is 8.22×10^6 m^3, while that of GM-ECBM recovery is 12.45×10^6 m^3, corresponding to an enhancement factor of 1.51.

4. Optimization of GM-ECBM recovery

The rationale for injecting the N_2:CO_2 gas mixture, rather than pure CO_2, is to avoid the significant reduction in reservoir permeability due to the CO_2-induced swelling. However, the excessive proportion of N_2 in the gas mixture may result in premature N_2 breakthrough in the production well. The high N_2 concentration in the produced gas flow will reduce the calorific value, thus forcing the premature shut-down of the production well. Therefore, key issues in optimizing the operation of GM-ECBM recovery, include: (i) how the gas production/storage performs under different Langmuir strain constants of CO_2 (ε_{L2}), and (ii) what reasonable compositions of CO_2 in the injected gas mixture (η_{CO2}) can be tolerated to maximize CH_4 recovery and the benefits of CO_2 sequestration.

The following investigation is completed with two scenarios representing injection at either constant-composition or with time-varying composition of the gases. Sensitivity studies are first applied to recover the optimized CO_2 composition for constant-composition injection with different CO_2 Langmuir strain constants (ε_{L2} = 0.0362,

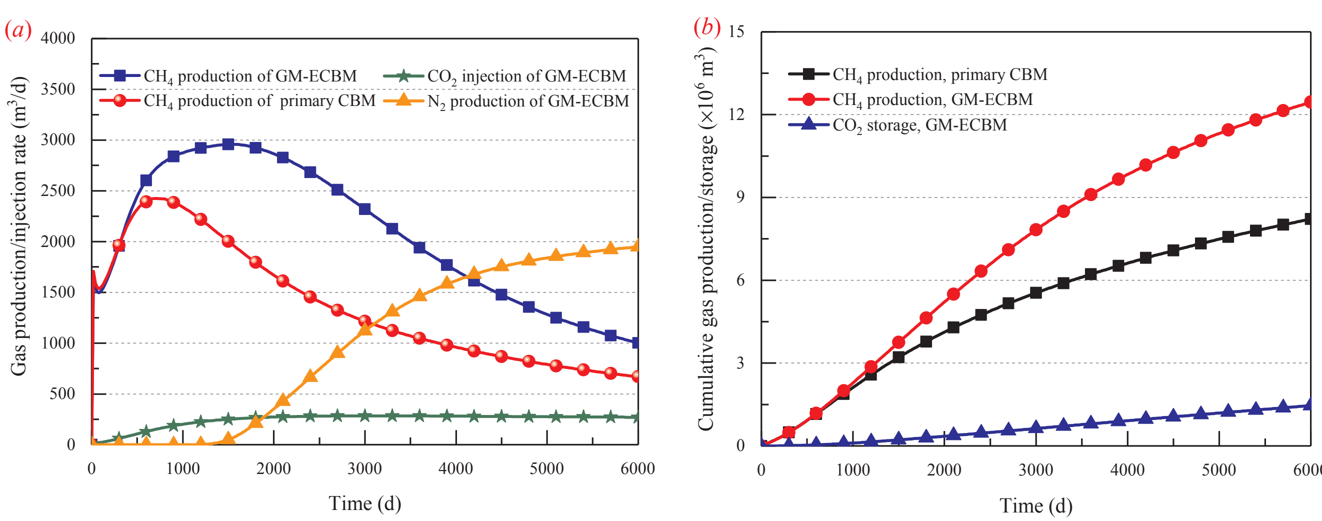

Fig. 10. Gas production and storage for primary and GM-ECBM recovery: (a) gas rate; (b) cumulative amount.

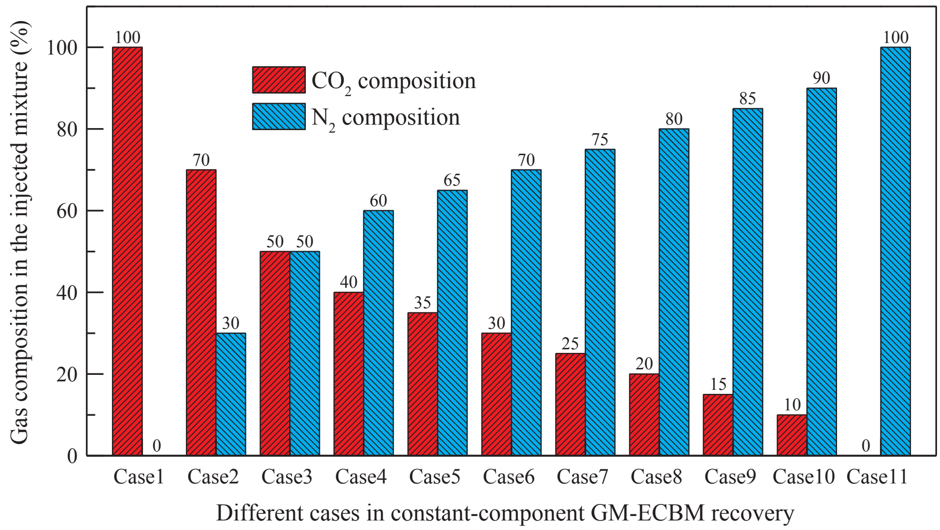

Fig. 11. Simulation schedules for constant-composition GM-ECBM recovery.

0.0482, 0.0602), followed by variable-composition injection with $\varepsilon_{L2} = 0.0362$.

4.1. Typical constant-composition gas mixture injection

The composition of the injected gas mixture is retained constant during the entire process of GM-ECBM recovery. According to the CO_2 composition in the injected mixture, the simulation schedule of constant-composition injection includes 11 cases, as shown in Fig. 11.

As N_2 has a low dynamic viscosity and adsorption capacity on coal, a higher N_2 (lower CO_2) composition greatly promotes the transport of N_2 in the coal seam, leading to early breakthrough of N_2 in produced gas flow. When the produced $N_2 + CO_2$ mixture reaches a threshold, the production well should be shut down. This threshold is defined as when the ratio of $N_2 + CO_2$ production rate to CH_4 production rate is equal to 50% (i.e., when $N_2 + CO_2$ fraction in the produced gas raises up to 33.3% by volume). Additionally, uneconomically low CH_4 production rates will result in the gas wells being shut down after 6000 days of production in the studied cases whether the threshold is reached or not.

Fig. 12 shows the CH_4 and $N_2 + CO_2$ production rates for different CO_2 Langmuir strain constants ($\varepsilon_{L2} = 0.0362$ (small swelling), 0.0482 (medium swelling), and 0.0602 (large swelling)). Both CH_4 and $N_2 + CO_2$ rates in the production well increases with the decrease in CO_2 composition. In Fig. 12(a), the peak CH_4 production rates for the injection of pure CO_2, flue gas (N_2:CO_2 = 85:15) and pure N_2 are 2574, 2958 and 3779 m^3/d, respectively. There is no $N_2 + CO_2$ gas flow in the production well before their breakthrough. After the arrival of the injected mixture, the production rate of $N_2 + CO_2$ increases rapidly, especially when the CO_2 composition is low. A greater CO_2 composition in the mixture corresponds to a smaller production rate of $N_2 + CO_2$.

We extract the CO_2 composition and the occurrence time of the shut-down threshold points for the different CO_2 Langmuir strain constants (ε_{L2}) in Fig. 12(a)–(c), and plot them in Fig. 13. A larger CO_2 composition corresponds to an increasingly delayed occurrence of the threshold point. For example, when $\varepsilon_{L2} = 0.0602$, the threshold occurs at 2200, 2920, 3520, 4420 and 5700 days for η_{CO2} = 0%, 10%, 15%, 20% and 25% respectively. With an increase in ε_{L2}, the CO_2 composition at threshold deceases. Specifically, the largest CO_2 compositions corresponding to $\varepsilon_{L2} = 0.0362$, 0.0482 and 0.0602 are 36.5%, 30.2% and 25.8% respectively, at the intersection of the extension line and unconditional shut down line (6000 days), as shown in Fig. 13.

Fig. 14 presents the relationship between the CO_2 composition and cumulative magnitudes of CH_4 production and CO_2, N_2 storage. With the CO_2 composition in the injected mixture increasing, the cumulative CH_4 production first inclines rapidly and then gradually declines. As a result, a greater Langmuir strain constant of CO_2 (ε_{L2}) leads to a smaller peak in cumulative CH_4 production. For example, the peak cumulative CH_4 production for $\varepsilon_{L2} = 0.0362$ is $10.58 \times 10^6\,m^3$, and the corresponding value for $\varepsilon_{L2} = 0.0602$ is $10.03 \times 10^6\,m^3$. Cumulative N_2 storage first decreases slowly then becomes more rapidly before finally slowing with the increase in CO_2 composition of the injected mixture.

As anticipated, the variation of cumulative CO_2 storage for different ε_{L2} varies widely. When the CO_2 composition in the injected gas mixture (η_{CO2}) < 20%, the CO_2 storages of $\varepsilon_{L2} = 0.0362$, 0.0482 and 0.0602 are all similar. However, when η_{CO2} > 20%, the variation of cumulative CO_2 storage differs significantly with an increase in CO_2 composition – the CO_2 storage for $\varepsilon_{L2} = 0.0362$ continuously increases, while that for both $\varepsilon_{L2} = 0.0482$ and 0.0602 increases first, followed by a slight decrease. This is because the excessive matrix swelling induced by CO_2 adsorption plays significant role in the sharp reduction in reservoir permeability near the injection well, and thus restricts the transport of the injected gas mixture. The higher the CO_2 composition in the injected mixture, the greater the impact of swelling induced by CO_2 adsorption on gas production/storage. For example, when pure (100%) CO_2 is injected into the coal seam, the cumulative CO_2 storages (6000 d) for $\varepsilon_{L2} = 0.0362$, 0.0482 and 0.0602 are 0.92, 2.37 and $7.78 \times 10^6\,m^3$ respectively. As shown in Fig. 14, the optimal CO_2 composition when the production well achieves maximum cumulative CH_4 recovery generally falls in the range of 20–40% depending on the coal swelling capacity to CO_2. For instance, the optimal CO_2 composition for $\varepsilon_{L2} = 0.0362$ is 35%.

4.2. Variable-composition gas mixture injection

We have previously discussed the effect of Langmuir strain constant of CO_2 on gas production/storage during constant-composition injection. Here, we select $\varepsilon_{L2} = 0.0362$ as a single base case to complete simulations of variable-composition injection to optimize the recovery schedule and maximize gas production/storage. The composition of the injected mixture is step-changed during the entire sequence of GM-ECBM recovery.

In this approach, the composition of the injected gas is changed after every period (step) of 1000 days. Defined by the variation of CO_2 composition of the injected mixture, the simulation schedule of variable-composition injection consists of 6 cases, e.g. Case 12: 90-70-50-35-20-10%, Case 13: 60-50-40-35-30-20%, Case 14: 50-45-40-35-30-25%, Case 15: 25-30-35-40-45-50%, Case 16: 20-30-35-40-50-60%,

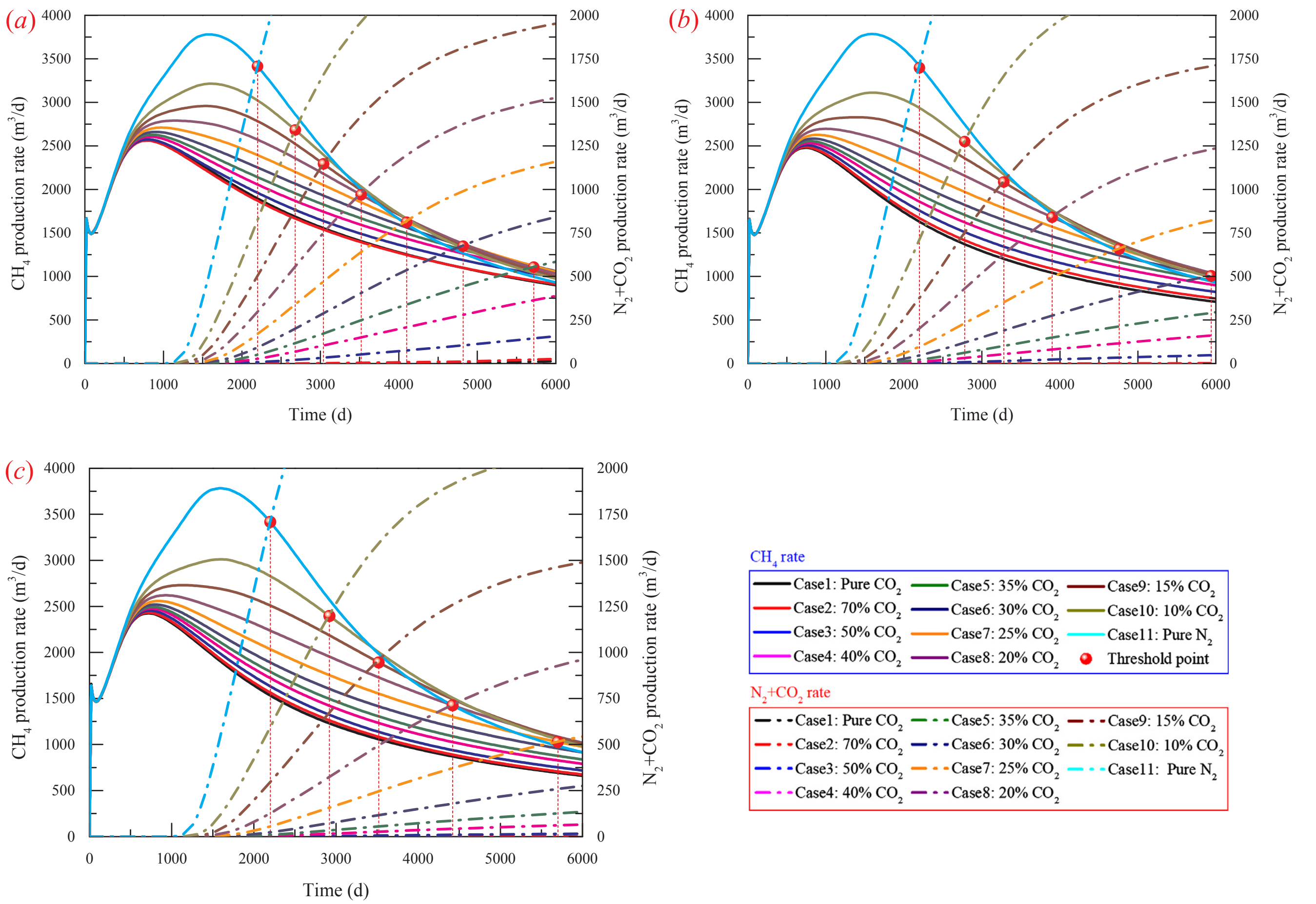

Fig. 12. Gas production rate for constant-composition gas injection for different Langmuir strain constants of CO_2: (a) $\varepsilon_{L2} = 0.0362$; (b) $\varepsilon_{L2} = 0.0482$, and (c) $\varepsilon_{L2} = 0.0602$ respectively.

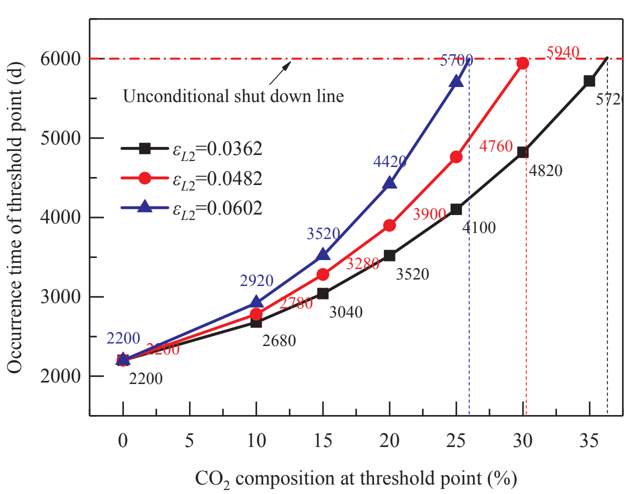

Fig. 13. The occurrence time and CO_2 composition of threshold points.

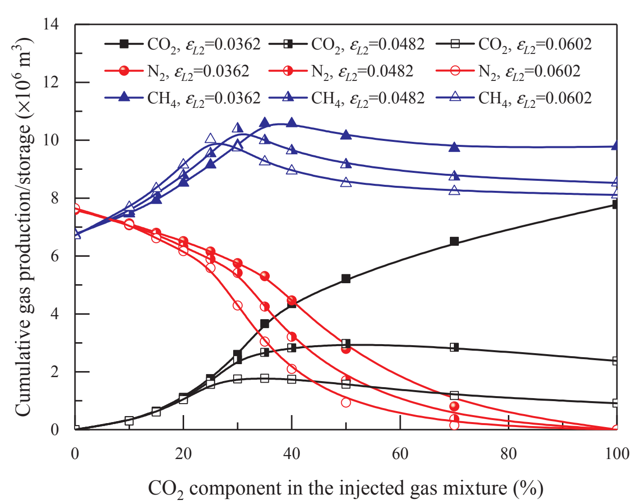

Fig. 14. Relationship between CO_2 composition in the injected mixture and cumulative gas production/storage.

Case 17: 10-20-35-50-70-90%, as shown in Fig. 15. Finally, the optimum schedules for both constant- and variable-composition injection are compared to evaluate the impacts of variable CO_2 composition on CH_4 production and CO_2 and N_2 sequestration.

Fig. 16 shows the variations of gas (CH_4, N_2 and CO_2) production rates during variable-composition GM-ECBM recovery. The CH_4 production rate for all cases has a similar trend during the dewatering stage, but after the reservoir is dewatered, the CH_4 production rates differ significantly between the various injection schedules. Cases 12–14 start with relatively high CO_2 composition that gradually decreases over subsequent time steps – these result in a correspondingly low early CH_4 production rate immediately following dewatering. Subsequently, the decrease in CO_2 composition results in an increase in CH_4 production rate and also a rapid increase in the $N_2 + CO_2$ production rate, resulting in early breakthrough of the injected mixture and early reaching of the shutdown threshold for the production well.

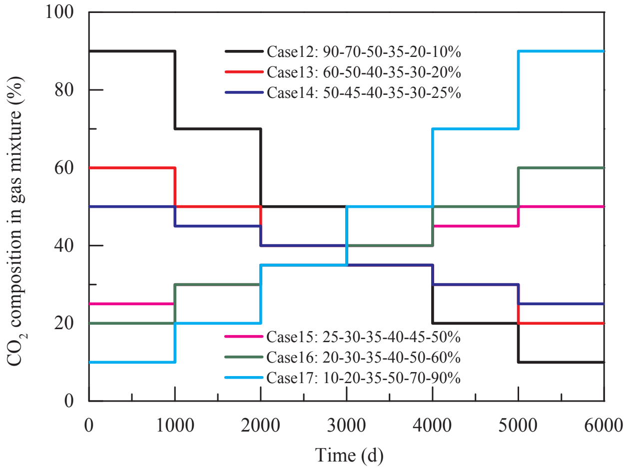

Fig. 15. Simulation scenarios for variable-composition GM-ECBM recovery.

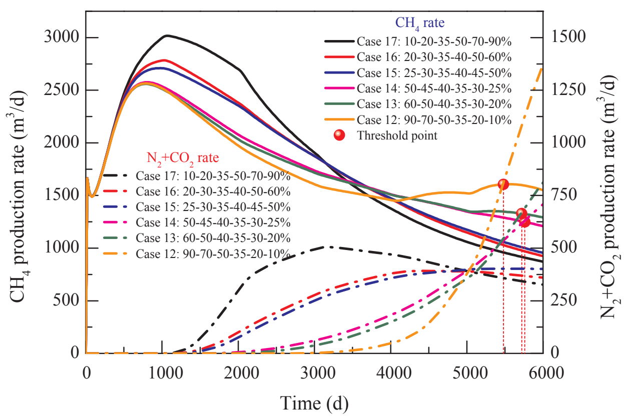

Fig. 16. Variation of gas (CH_4, N_2, CO_2) production rate during varying-composition GM-ECBM recovery.

Cases 15–17 begin with a relatively low CO_2 composition and continue with gradual increase in CO_2 concentration. In this case, the displaced CH_4 is driven by injected N_2 flow towards the production well, and results in a rapid enhancement in early production immediately following dewatering. In Fig. 16, the CH_4 production rate of cases 15–17 increases to relatively high levels early in production. As the CO_2 composition in the injected gas mixture increases, reservoir permeability rapidly decreases due to excessive matrix swelling, leading to a sharp decrease in $N_2 + CO_2$ production rate. Consequently, the shutdown threshold for production well is not reached until the end of production (6000 days).

As illustrated in Fig. 17, injection sequences that begin with a low CO_2 composition that gradually increases, provides an optimal balance between reaching an early shut-down N_2 threshold and excessive matrix swelling induced by CO_2 adsorption – this results in a prolonged the production time. The maximum cumulative CH_4 production ($11.26 \times 10^6\,m^3$) and CO_2 sequestration ($7.78 \times 10^6\,m^3$) are obtained in a single injection schedule – case 17 (10–20–35–50–70–90% CO_2). Thus, case 17 is the preferred injection schedule among all the simulated cases for the variable composition GM-ECBM recovery.

The cumulative CH_4 production volumes and recovery ratios for the different CBM recovery schedules are listed in Table 3. The recovery ratio for primary CBM recovery is 49.91% compared to the recovery ratio for pure N_2-ECBM at only 41.04%. This indicates that pure N_2-ECBM may be ineffective at promoting CH_4 recovery from coal seams, due to its early breakthrough and early attainment of shut-down threshold in the production well. Comparing with primary CBM recovery, the recovery ratios of pure CO_2, optimal constant injection and

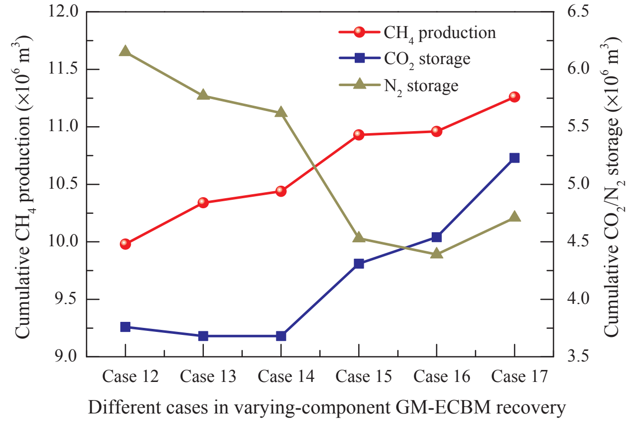

Fig. 17. Cumulative CH_4 production and CO_2/N_2 storage for different cases of varying CO_2-composition in injected mixture.

optimal variable injection are 59.4%, 64.2% and 68.4%, with enhancement ratios of 1.19, 1.29 and 1.37, respectively. This illustrates that the approach of variable composition injection for GM-ECBM recovery is an effective method to improve coalbed methane production. And the model exercised in this work provides a rational means to define controlling processes and resulting responses.

Note that the optimal composition of the injected gas will vary among different sites and geological conditions, and the impacts of well spacing, injection pressures and other parameters, including the definition of economic conditions controlling recovery. However, an optimal variable-composition schedule for gas mixture injection can always be determined according to the actual situation.

5. Conclusions

An improved thermo-hydro-mechanical (THM) model is developed to couple the responses of coal deformation, mass transport of a mixture of ternary gases (CH_4, CO_2 and N_2) and water together with heat transfer. This model is first validated then applied to simulate gas-mixture enhanced coalbed methane (GM-ECBM) recovery. Sensitivity analyses are conducted on the control of key parameters together with optimization of recovery schedules. These simulations provide an improved understanding on the processes controlling GM-ECBM recovery. The following conclusions are drawn:

(1) Injection of gas mixture (CO_2, N_2) significantly promotes coalbed methane recovery. This is reflected in an elevated peak production rate and an increased cumulative production. Both CH_4 pressure and content decrease rapidly at early time due to the displacement of the injected gas followed by a slowing in this rate.
(2) As gas pressure drops due to production, CH_4 desorption-induced heat dissipation increases, resulting in a continuous decrease in reservoir temperature near the production well. This is complemented by a rapid temperature increase at the injection well due to the injection of the hot recovery gas. The sweep of N_2 accelerates CH_4 desorption and subsequent transport, and hence promotes a decrease in reservoir temperatures distant from the injection well even prior to the arrival of CO_2.
(3) Permeability evolution is controlled by both gas mixture injection and methane production. Before the arrival of the CO_2/N_2 mixture front, permeability increase is dominated by CH_4 desorption-induced shrinkage. After the arrival of the front, permeability is dominated by competitive result of CH_4 desorption-induced shrinkage and N_2:CO_2 adsorption-induced swelling. As a result, a rapid increase in permeability in the early stages is followed by a dramatic decrease at later stages.
(4) An increased Langmuir strain constant to CO_2 reduces critical

Table 3
Comparison of gas recovery between different recovery schedules.

Recovery schedules	CO_2 composition in injected mixture (%)	Cumulative CH_4 production ($\times 10^6 m^3$)	Gas recovery ratio (%)
Primary CBM	——	8.22	49.9
Pure N_2-ECBM	0	6.76	41.0
Pure CO_2-ECBM	100	9.78	59.4
Optimal constant GM-ECBM	35	10.58	64.2
Optimal varying GM-ECBM	10–20-35–50–70–90	11.26	68.4

compositions of CO_2 in the injected mixture required to reach the threshold for well shut down. The optimal CO_2 composition for constant-composition GM-ECBM generally falls in the range of 20–40% depending on coal swelling susceptibility to CO_2. Beginning with injection of low CO_2 composition, following by a sequential increase (of CO_2 composition), results in an optimal balance between avoiding the reaching of an early threshold (N_2) and large matrix swelling (CO_2). Of the case studied, the gas recovery ratio of optimal variable-composition mixture/schedule is 68.4% compared to 64.2% of constant-composition, illustrating the superiority of variable-composition injection during GM-ECBM recovery.

The fully coupled THM model developed in this work not only offers useful framework to investigate important technical challenges associated GM-ECBM, but can also be applied to other forms of unconventional gas extraction, and other fields such as CO_2 geological sequestration, underground coal gasification, and geothermal development.

Acknowledgments

The author(s) thank the editors and anonymous reviewers for their comments and suggestions. This research was financially supported by the National Natural Science Foundation of China (Grant Nos. 51674132 and 51874159), the Research Fund of State Key Laboratory Cultivation Base for Gas Geology and Gas Control (Henan Polytechnic University) (Grant No. WS2018B05), the Basic Research Project of Key Laboratory of Liaoning Provincial Education Department (Grant No. LJZS004), and the Postdoctoral Science Foundation of China (Grant No. 2018M641675).

Notes

The authors declare no competing financial interest.

References

[1] Wang H, Cheng Y, Wang W, Xu R. Research on comprehensive CBM extraction technology and its applications in China's coal mines. J Nat Gas Sci Eng 2014;20:200–7.
[2] Wu Y, Pan Z, Zhang D, Lu Z, Connell LD. Evaluation of gas production from multiple coal seams: a simulation study and economics. Int J Min Sci Technol 2018;28:359–71.
[3] Yin G, Deng B, Li M, Zhang D, Wang W, Li W, et al. Impact of injection pressure on CO2–enhanced coalbed methane recovery considering mass transfer between coal fracture and matrix. Fuel 2017;196:288–97.
[4] Aguado MBD, Nicieza CG. Control and prevention of gas outbursts in coal mines, Riosa-Olloniego coalfield Spain. Int J Coal Geol 2007;69(4):253–66.
[5] Liu T, Lin B, Zou Q, Zhu C. Microscopic mechanism for enhanced coal bed methane recovery and outburst elimination by hydraulic slotting: a case study in Yangliu mine China. Greenhouse Gases 2016;6(5):597–614.
[6] Sobczyk J. A comparison of the influence of adsorbed gases on gas stresses leading to coal and gas outburst. Fuel 2014;115:288–94.
[7] Li S, Fan C, Han J, Luo M, Yang Z, Bi H. A fully coupled thermal-hydraulic-mechanical model with two-phase flow for coalbed methane extraction. J Nat Gas Sci Eng 2016;33:324–36.
[8] Thararoop P, Karpyn ZT, Ertekin T. Development of a multi-mechanistic, dual-porosity, dual-permeability, numerical flow model for coalbed methane reservoirs. J Nat Gas Sci Eng 2012;8:121–31.
[9] Mazzotti M, Pini R, Storti G. Enhanced coalbed methane recovery. J Supercrit Fluid 2009;47(3):619–27.
[10] Zhang S, Liu L, Zhang L, Zhuang Y, Du J. An optimization model for carbon capture utilization and storage supply chain: a case study in Northeastern China. Appl Energy 2018;231:194–206.
[11] Shi JQ, Durucan S, Fujioka M. A reservoir simulation study of CO2 injection and N2 flooding at the Ishikari coalfield CO2 storage pilot projectJapan. Int J Greenhouse Gas Control 2008;2(1):47–57.
[12] Zhou F, Hou W, Allinson G, Wu J, Wang J, Cinar Y. A feasibility study of ECBM recovery and CO2 storage for a producing CBM field in Southeast Qinshui Basin China. Int J Greenh Gas Control 2013;19:26–40.
[13] Lin J, Ren T, Wang G, Nemcik J. Simulation investigation of N2-injection enhanced gas drainage: model development and identification of critical parameters. J Nat Gas Sci Eng 2018;55:30–41.
[14] Huang Y, Zheng QP, Fan N, Aminian K. Optimal scheduling for enhanced coal bed methane production through CO2 injection. Appl Energy 2014;113:1475–83.
[15] Aminu MD, Nabavi SA, Rochelle CA, Manovic V. A review of developments in carbon dioxide storage. Appl Energy 2017;208:1389–419.
[16] Wen H, Li Z, Deng J, Shu CM, Laiwang B, Wang Q, et al. Influence on coal pore structure during liquid CO2-ECBM process for CO2 utilization. J CO2 Util 2017;21:543–52.
[17] Stevens SH, Spector D, Riemer P. Enhanced coalbed methane recovery using CO2 injection: worldwide resource and CO2 sequestration potential. In: SPE International Oil and Gas Conference and Exhibition in China. Soc. Pet. Eng. 1998. SPE-48881-MS.
[18] Sınayuç Ç, Gümrah F. Modeling of ECBM recovery from Amasra coalbed in Zonguldak Basin Turkey. Int J Coal Geol 2009;77(1–2):162–74.
[19] Sayyafzadeh M, Keshavarz A, Alias ARM, Dong KA, Manser M. Investigation of varying-composition gas injection for coalbed methane recovery enhancement: a simulation-based study. J Nat Gas Sci Eng 2015;27:1205–12.
[20] Durucan S, Ahsanb M, Shia JQ. Matrix shrinkage and swelling characteristics of European coals. Energy Procedia 2009;1(1):3055–62.
[21] Song Y, Jiang B, Qu MJ. Molecular dynamic simulation of self-and transport diffusion for CO2/CH4/N2 in low-rank coal vitrinite. Energy Fuel 2018;32(3):3085–96.
[22] Song Y, Jiang B, Lan FJ. CompetitivSe adsorption of CO2/N2/CH4 onto coal vitrinite macromolecular: Effects of electrostatic interactions and oxygen functionalities. Fuel 2019;235:23–38.
[23] Cui X, Bustin RM. Volumetric strain associated with methane desorption and its impact on coalbed gas production from deep coal seams. AAPG Bull 2005;89(9):1181–202.
[24] Durucan S, Shi JQ. Improving the CO2 well injectivity and enhanced coalbed methane production performance in coal seams. Int J Coal Geol 2009;77(1–2):214–21.
[25] Zhou F, Hussain F, Cinar Y. Injecting pure N2 and CO2 to coal for enhanced coalbed methane: experimental observations and numerical simulation. Int J Coal Geol 2013;116:53–62.
[26] Zhang XG, Ranjith PG, Li DY, Perera MSA, Ranathunga AS, Zhang BN. CO2 enhanced flow characteristics of naturally-fractured bituminous coals with N2 injection at different reservoir depths. J CO2 Util 2018;28:393–402.
[27] Fujioka M, Yamaguchi S, Nako M. CO2-ECBM field tests in the Ishikari coal basin of Japan. Int J Coal Geol 2010;82(3–4):287–98.
[28] Fang Z, Li X, Hu H. Gas mixture enhance coalbed methane recovery technology: pilot tests. Energy Procedia 2011;4:2144–9.
[29] Durucan S, Ahsan M, Syed A, Shi JQ, Korre A. Two phase relative permeability of gas and water in coal for enhanced coalbed methane recovery and CO2 storage. Energy Procedia 2013;37:6730–7.
[30] Rutqvist J, Wu YS, Tsang CF, Bodvarsson G. A modeling approach for analysis of coupled multiphase fluid flow, heat transfer, and deformation in fractured porous rock. Int J Rock Mech Min Sci 2002;39(4):429–42.
[31] Zheng C, Lin B, Kizil MS, Aminossadati SM, Li H, Chen Z. Analysis on the multiphase flow characterization in cross-measure borehole during coal hydraulic slotting. Int J Min Sci Technol 2018;28:701–5.
[32] Liu T, Lin B, Yang W. Impact of matrix–fracture interactions on coal permeability: model development and analysis. Fuel 2017;207:522–32.
[33] Jessen K, Tang GQ, Kovscek AR. Laboratory and simulation investigation of enhanced coalbed methane recovery by gas injection. Transport Porous Med 2008;73(2):141–59.
[34] Fang Z, Li X, Wang GGX. A gas mixture enhanced coalbed methane recovery technology applied to underground coal mines. J Min Sci+ 2013;49(1):106–17.
[35] Shi JQ, Durucan S. A bidisperse pore diffusion model for methane displacement desorption in coal by CO2 injection. Fuel 2003;82(10):1219–29.
[36] Zhang XG, Ranjith PG, Perera MSA, Ranathunga AS, Haque A. Gas transportation and enhanced coalbed methane recovery processes in deep coal seams: a review. Energy Fuel 2016;30(11):8832–49.
[37] Sun X, Zhang Y, Li K, Gai Z. A new mathematical simulation model for gas injection enhanced coalbed methane recovery. Fuel 2016;183:478–88.
[38] Durucan S, Shi JQ. Improving the CO2 well injectivity and enhanced coalbed methane production performance in coal seams. Int J Coal Geol 2009;77:214–21.

[39] Wu Y, Liu J, Chen Z, Elsworth D, Pone D. A dual poroelastic model for CO2-enhanced coalbed methane recovery. Int J Coal Geol 2011;86(2):177–89.
[40] Ren T, Wang G, Cheng Y, Qi Q. Model development and simulation study of the feasibility of enhancing gas drainage efficiency through nitrogen injection. Fuel 2017;194:406–22.
[41] Zhu WC, Wei CH, Liu J, Qu HY, Elsworth D. A model of coal–gas interaction under variable temperatures. Int J Coal Geol 2011;86(2):213–21.
[42] Guan C, Liu S, Li C, Wang Y, Zhao Y. The temperature effect on the methane and CO2 adsorption capacities of Illinois coal. Fuel 2018;211:241–50.
[43] Teng T, Zhao Y, Gao F, Wang JG, Wang W. A fully coupled thermo-hydro-mechanical model for heat and gas transfer in thermal stimulation enhanced coal seam gas recovery. Int J Heat Mass Transfer 2018;125:866–75.
[44] Ma T, Rutqvist J, Oldenburg CM, Liu W, Chen J. Fully coupled two-phase flow and poromechanics modeling of coalbed methane recovery: impact of geomechanics on production rate. J Nat Gas Sci Eng 2017;45:474–86.
[45] Fan Y, Deng C, Zhang X, Li F, Wang X, Qiao L. Numerical study of CO2-enhanced coalbed methane recovery. Int J Greenhouse Gas Control 2018;76:12–23.
[46] Sayyafzadeh M, Keshavarz A. Optimisation of gas mixture injection for enhanced coalbed methane recovery using a parallel genetic algorithm. J Nat Gas Sci Eng 2016;33:942–53.
[47] Reeves S, Oudinot A. The Tiffany Unit N2-ECBM Pilot: A Reservoir Modeling Study. Advanced Resources International, Incorporated 2004.
[48] Liu T, Lin B, Yang W, Zhai C, Liu T. Coal permeability evolution and gas migration under non-equilibrium state. Transport Porous Med 2017;118(3):393–416.
[49] Fan CJ, Li S, Luo MK, Yang ZH, Lan TW. Numerical simulation of hydraulic fracturing in coal seam for enhancing underground gas drainage. Energy Explor Exploit 2018:1–28. https://doi.org/10.1177/0144598718785998.
[50] Wang G, Wang K, Wang S, Elsworth D, Jiang Y. An improved permeability evolution model and its application in fractured sorbing media. J Nat Gas Sci Eng 2018;56:222–32.
[51] Elsworth D, Bai M. Flow-deformation response of dual-porosity media. J Geotech Eng. 1992;118:107–24.
[52] Wu F, Chen J, Zou Q. A nonlinear creep damage model for salt rock. Int J Damage Mech 2018:1–14.
[53] Lim KT, Aziz K. Matrix–fracture transfer shape factors for dual-porosity simulators. J Petrol Sci Eng 1995;13(3):169–78.
[54] Corey AT. The interrelation between gas and oil relative permeability. Prod Mon 1954;31:533–46.
[55] Bertrand F, Cerfontaine B, Collin F. A fully coupled hydro-mechanical model for the modeling of coalbed methane recovery. J Nat Gas Sci Eng 2017;46:307–25.
[56] Clarkson CR, Rahmanian M, Kantzas A, Morad K. Relative permeability of CBM reservoirs: controls on curve shape. Int J Coal Geol 2011;88(4):204–17.
[57] Tao S, Tang D, Xu H, Gao L, Fang Y. Factors controlling high-yield coalbed methane vertical wells in the Fanzhuang Block, Southern Qinshui Basin. Int J Coal Geol 2014;134:38–45.
[58] Engineeringtoolbox. https://www.engineeringtoolbox.com/.
[59] Chen D, Pan Z, Liu J, Connell LD. An improved relative permeability model for coal reservoirs. Int J Coal Geol 2013;109:45–57.
[60] Fan C, Elsworth D, Li S, Zhou L, Yang Z, Song Y. Thermo-hydro-mechanical-chemical couplings controlling CH4 production and CO2 sequestration in enhanced coalbed methane recovery. Energy 2019;173:1054–77.